Climate Dynamics (2024) 62:2475–2498
https://doi.org/10.1007/s00382-023-07034-9

ORIGINAL ARTICLE

CMIP6 precipitation and temperature projections for Chile

Álvaro Salazar[1,2] · Marcus Thatcher[3] · Katerina Goubanova[4] · Patricio Bernal[5] · Julio Gutiérrez[1,2,4] · Francisco Squeo[1,2,4]

Received: 1 June 2023 / Accepted: 18 November 2023 / Published online: 22 December 2023

Abstract
Precipitation and near-surface temperature from an ensemble of 36 new state-of-the-art climate models under the Coupled Model Inter-comparison Project phase 6 (CMIP6) are evaluated over Chile's climate. The analysis is focused on four distinct climatic subregions: Northern Chile, Central Chile, Northern Patagonia, and Southern Patagonia. Over each of the subregions, first, we evaluate the performance of individual global climate models (GCMs) against a suit of precipitation and temperature observation-based gridded datasets over the historical period (1986–2014) and then we analyze the models' projections for the end of the century (2080–2099) for four different shared socioeconomic pathways scenarios (SSP). Although the models are characterized by general wet and warm mean bias, they reproduce realistically the main spatiotemporal climatic variability over different subregions. However, none of the models is best across all subregions for both precipitation and temperature. Moreover, among the best performing models defined based on the Taylor skill score, one finds the so-called "hot models" likely exhibiting an overestimated climate sensitivity, which suggests caution in using these models for accessing future climate change in Chile. We found robust (90% of models agree in the direction of change) projected end-of-the-century reductions in mean annual precipitation for Central Chile (~ − 20 to ~ − 40%) and Northern Patagonia (~ − 10 to ~ − 30%) under scenario SSP585, but changes are strong from scenario SSP245 onwards, where precipitation is reduced by 10–20%. Northern Chile and Southern Patagonia show non-robust changes in precipitation across the models. Yet, future near-surface temperature warming presented high inter-model agreement across subregions, where the greatest increments occurred along the Andes Mountains. Northern Chile displays the strongest increment of up to ~ 6 °C in SSP585, followed by Central Chile (up to ~ 5 °C). Both Northern and Southern Patagonia show a corresponding increment by up to ~ 4 °C. We also briefly discuss about the environmental and socio-economic implications of these future changes for Chile.

Keywords General circulation models · IPCC · South America · Andes · Climate projections · Chile

1 Introduction

With the advent of the Coupled Model Inter-comparison Project phase 6 (CMIP6) multimodel ensemble (Eyring et al. 2016), new opportunities arise to investigate the climate system at global and regional scales under a series of future emission scenarios. CMIP6 builds upon previous CMIP5, which are fundamental inputs to the Intergovernmental Panel on Climate Change (IPCC) Assessment Reports, AR6 and AR5 (IPCC 2013, 2021), respectively. It presents a new framework of socioeconomic scenarios, named Shared Socioeconomic Pathways (SSP), that are combined with the Representative Concentration Pathways (RCP) of CMIP5 (Eyring et al. 2016; Meinshausen et al. 2020). This new generation of climate models is of great value for evaluating future climate evolution in Chile, which appears as one of the world's regions most sensitive to changes in climate (Ukkola et al. 2020).

An increasing number of studies are identifying some improvements of CMIP6 compared to previous CMIP ensembles. The new generation of models can better

✉ Álvaro Salazar
alvaro.salazar.p@gmail.com

1 Institute of Ecology and Biodiversity (IEB), Victoria 631, Barrio Universitario, Concepción, Chile

2 Departamento de Biología, Facultad de Ciencias, Universidad de La Serena, Casilla 554, La Serena, Chile

3 CSIRO Environment, Aspendale, VIC 3195, Australia

4 Centro de Estudios Avanzados en Zonas Áridas (CEAZA), La Serena, Chile

5 CSIRO Chile Research Foundation, Santiago, Chile

reproduce large-scale patterns of climate for specific variables and correct the wet bias identified in previous CMIP generations for western South America (Rivera and Arnould 2020), Australian climate (Grose et al. 2020), precipitation in North America (Akinsanola et al. 2020), the spatiotemporal pattern of monsoon over India (Gusain et al. 2020), China and East Asia (Xin et al. 2020), West Africa (Faye and Akinsanola 2022), the Mediterranean region (Cos et al. 2022) and areas of Southeast Asia (Ge et al. 2021; Try et al. 2022). However, the latest generation of models conforming to the CMIP6 ensemble still has limitations in the representation of some climate processes, and projections must be studied considering their uncertainties. Sources of uncertainties in GCMs are due to model resolution and physics, which can affect the description of subgrid convective heat transfer that is especially relevant in mountainous areas (Foley 2010; Peng et al. 2022). Additional uncertainties can result from unknown future human influences on the climate system such as land-surface feedback changes from land use/cover transitions, technological advances and population growth (IPCC 2022). The complexity, multiplicity and nonlinear nature of the processes and feedbacks that the climate system contains, obstacles its faithful representation in GCMs (Ghil 2020; Ghil et al. 2008; Knutti et al. 2008).

A significant number of models of CMIP6 also present a new attribute not seen in the previous CMIPs ensembles as they likely overestimate equilibrium climate sensitivity (Tokarska et al. 2020). Equilibrium climate sensitivity (ECS) is a tractable manner to characterize the temperature response of the Earth to a change in CO2 forcing, which depends on several feedback processes such as those associated with water vapor, lapse rate, surface albedo and clouds (Knutti and Rugenstein 2015). The ECS of the CMIP5 models varied from 2.1 to 4.5 °C; and the IPCC AR5 report in 2013 estimated that it likely ranges from 1.5 to 4.5 °C (IPCC 2013). However, the ECS of some of the new CMIP6 GCMs presents an ECS greater than 5 °C, which can lead the models to project a warming that is greater than expected based on multiple lines of evidence (IPCC 2022). This warming can be traced to a positive net cloud feedback that is larger in CMIP6 compared to CMIP5 by 20% (IPCC 2022). The critical question is whether future warming projections of such models are realistic or current climate assessments need to recalibrate the raw ensemble or select a subset of low-sensitive models (Tokarska et al. 2020). In our study, we present all available results from CMIP6 GCMs, yet we track those highly sensitive models detected by recent studies (Scafetta 2022; Tokarska et al. 2020).

The investigation of Chile's future climate is of great interest. First, it strides along ~ 4000 km alongside the west coast of South America and therefore presents a set of distinct climate zones with a marked north–south precipitation gradient ranging from the hyper-arid Atacama Desert in the north to polar climate near Antarctica. Mediterranean and Temperate climates extend between these extremely dry/hot and wet/cold climates (Beck et al. 2018). The presence of the Andes Mountains adds additional complexity to the regional climate system with elevations reaching up to ~ 7000 m a.s.l. The Andes produces a strong orographic enhancement of synoptic-scale precipitation upstream of the mountains (Garreaud 2009; Garreaud et al. 2013; Massmann et al. 2017; Viale and Garreaud 2014). In the Chilean Patagonia, this enhancement can produce annual total precipitation as high as ~ 6000 mm and can decrease to less than 100 mm within 100 km east of the Andes (Garreaud 2009; Viale et al. 2019). These features challenge the ability of coarse-resolution climate models' simulations to resolve local-scale characteristics produced by orographic forcing. They also hinder the ability of proper validation of such simulations due to a scarce ground observational network, in particular over areas of complex topography and extremely dry and wet climates (Bozkurt et al. 2019). Therefore, it is necessary to evaluate the performance of the new set of GCMs over these highly heterogeneous areas not currently recognized as distinct climatic zones by Intergovernmental Panel on Climate Change reference subregions (Almazroui et al. 2021; Iturbide et al. 2020).

Second, Chile is a climate-change hotspot because it has shown to be very sensitive to global change, with a drying trend that is expected to continue in the coming future (Boisier et al. 2018; Garreaud et al. 2020). A large proportion of south-Central Chile has experienced a consistent decreasing precipitation trend since the late 1970s that is attributable both to natural climate variability (e.g., Pacific Decadal Oscillation) and anthropogenic warming (Boisier et al. 2018, 2016; Quintana and Aceituno 2012). Since 2010, Central Chile has registered precipitation deficits ranging from 25 to 45%, with impacts on the Andean snowpack and declines up to 90% in river flow, reservoir volumes, and groundwater levels (Garreaud et al. 2017). This trend is particularly relevant for snow-dominated catchments, which accumulate the effects of precipitation deficits caused by persistent drought conditions and provide less water for people and ecosystems (Alvarez-Garreton et al. 2021). The warmer and drier trend is also affecting snow cover of northern Chile (Schauwecker et al. 2023), glaciers mass loss across the country (Ayala et al. 2020; Dussaillant et al. 2019; Feron et al. 2019; Pellicciotti et al. 2014; Vuille et al. 2018), and incrementing the frequency and magnitude of dry season wildfires in Central and South-Central Chile with catastrophic impacts over natural and rural areas (González et al. 2018; Urrutia-Jalabert et al. 2018). Future projections of precipitation and temperature using CMIP ensembles, particularly in the Andes, project a scenario-dependent enhancement of the current trends (Zazulie et al. 2018; Pabón-Caicedo et al. 2020). In Central Chile, Bozkurt et al. (2018) used 19 GCMs from

CMIP5 adjusted with observations and predicted a drying of ~ − 3% (RCP2.6), ~ − 30% (RCP8.5) and a warming of ~ + 1.2 ◦C (RCP2.6), ~ + 3.5 ◦C (RCP8.5) by the end of the century, leading to a decrease in annual runoff of about 40% in the RPC8.5 scenario. More recently, Aguayo et al. (2021) explored a set of GCMs from CMIP5 and CMIP6 in combination to hydrological modelling. Their results project an increase in the duration, hydrological deficit, and frequency of severe droughts of varying duration towards the 2040–2070 period that agrees with previous studies (Araya-Osses et al. 2020; Penalba and Rivera 2016). Mardones and Garreaud (2020) also showed that the future temperature change for scenario RCP8.5 is associated with an upward shift of snow-rain transition of 400–600 m, increasing the risk of landslides and flashfloods along the foothills of the subtropical Andes. The vast majority of these studies have been directed to south Central Chile whereas results of climate projections for the extreme north and south of Chile are fraught with uncertainties.

In this study, we analyze the climate projections over Chile at the end of the century (2080–2099) with respect to the historical period (1986–2014) in a set of 36 CMIP6 GCMs under four emission scenarios. We accounted for the heterogeneity in climate characteristics by dividing Chile into four distinct subregions: Northern Chile, Central Chile, Northern Patagonia, and Southern Patagonia. Over each of these subregions, we compare the historical simulations against a suit of gridded observation datasets and further analyze the distribution of the simulated mean annual precipitation and near-surface temperature across space and time in the present and future climate.

2 Data and methodology

2.1 Study area

Our study area comprises the coastal and continental extension of Chile from parallel 17.5°S to 56°S (~4250 km extension). Based on Iturbide et al. (2020), we redefined their IPCC reference regions of south-western South America and southern South America to new four subregions for Chile: Northern Chile, Central Chile, Northern Patagonia, and Southern Patagonia (Fig. 1). These subregions present distinct climatic features that are wide enough to assess results from CMIP6 models. Northern Chile (17.5–29°S) covers the Atacama Desert. This subregion is characterized by a hyper-arid climate defined by a large-scale subsidence over the subtropical southeast Pacific Ocean and low sea surface temperature off Chile and Perú (Garreaud et al. 2010, 2009). Driest conditions occur near the coast and low elevation zones (≤ 1000 m ASL) with increasing summer precipitation (DJF) at higher elevations (> 3000 m ASL) due to moisture transport from lowland areas east of the Andes (Garreaud et al. 2003). Central Chile (29–40°S) has a typical Mediterranean climate with stratiform winter precipitation (JJA). Its climate is shaped by the subtropical anticyclone and the storm track at midlatitudes (Garreaud et al. 2009, 2017), with a marked meridional precipitation gradient forced by mechanical lift leading to an orographic precipitation enhancement by a factor 1.8 ± 0.3 from the coast to the western Andean slopes between 33 and 44°S (Viale and Garreaud 2015; Garreaud et al. 2017). As in the previous subregion, Northern Patagonia's (40–47°S) temperate climate is influenced by the subtropical anticyclone and the circumpolar ring of midlatitude westerlies intersecting South America between 40 and 50°S (Garreaud and Aceituno 2007). High continental precipitation rates of Northern Patagonia subside at about parallel 47°S, where cooler polar conditions influence climate, and the tundra biome begins to dominate (Aguirre et al. 2021; Beck et al. 2018). In the present study, this change is considered the start of Southern Patagonia (47–56°S), where the polar climate is influenced by the circumpolar low-pressure belt surrounding Antarctica around 60°S and the seasonal displacement of the subtropical anticyclone. These features modulate eastward frontal precipitation, resulting in greater total precipitation but at lower rates than over the northern neighbor region. Southern Patagonia exhibits a distinct zonal asymmetry, with wet conditions alongside the west coast and drier/cold conditions towards the east (Fig. 6a).

2.2 Data

In this study, we set as the reference climate the 1986–2014 period. For this period, we included monthly observational data for precipitation and near-surface temperature from different sources (summarized in Table 1). Based on the availability at the time of writing, we assessed projected monthly mean precipitation and temperature using 36 CMIP6 Global Climate Models (GCMs, listed in Table 2). The focus was directed to the subregional mean annual changes in the late-century period of 2080–2099 relative to the reference period for four future scenarios, namely SSP1-2.6 (SSP126), SSP2-4.5 (SSP245), SSP3-7.0 (SSP370) and SSP5-8.5 (SSP585). We considered only one member (r1i1p1f1), and all models were weighted equally. Using conservative remapping, all models and observations were re-gridded to a common 1° × 1° lat/lon resolution.

2.3 Evaluation

For each subregion, we evaluated CMIP6 GCMs against the arithmetic mean of observation datasets (ensemble mean). Because observational temperature datasets were restricted to land, we processed this field for land grid

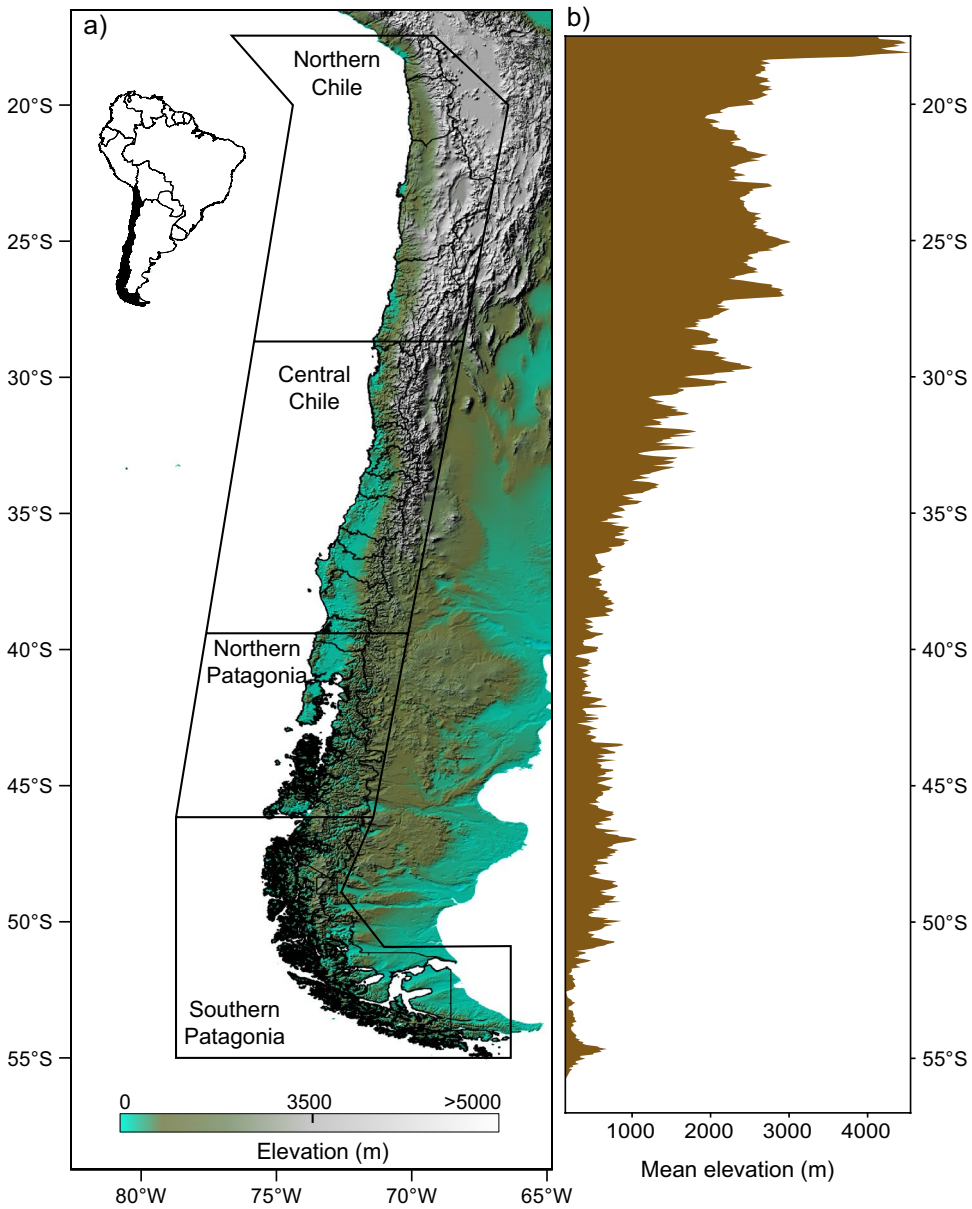

Fig. 1 **a** Study area divided in four subregions and **b** corresponding mean elevation by latitude

points only. On the contrary, precipitation was processed for the entire domain of each subregion including land and ocean. The spatiotemporal performance of individual models for precipitation and temperature was assessed using a set of statistical metrics. We addressed the annual cycle of GCMs using Fourier transform equations. The amplitude and phase of annual cycle was estimated by fitting the annual Fourier harmonic (Ding et al. 2023; Hu et al. 2022) to the monthly series that were previously smoothed using spline cubic functions. To appraise how well the Fourier transform effectively describes the seasonal cycle of the monthly series, we evaluated the performance of Fourier predictions against the original precipitation and temperature data across space and time for each of the studied subregions. Then we used the Fourier method to fit all series (observations and GCMs) and used their trigonometric properties to compare amplitude and climatological peak month. The mean bias error MBE was calculated as the mean distance between the climatological normal of models and observations in units of the observed mean field (Willmott 1982). The normalized root mean square error NRMSE was calculated after normalizing the root mean square error by the observations, and it was chosen because it is more suitable when values differ in order of magnitude (Guo et al. 2021). A smaller value of MBE and NRMSE reflects a closer fit to observations for the respective GCM. The equations of MBE and NRMSE are given as follows:

Table 1 Gridded observations used in this study

Variable	Dataset	Method	Resolution (°)	Source
Precipitation	CHIRPS v2.0 (Climate Hazards group Infrared Precipitation with Stations)	Satellite + Gauge	0.05	https://www.chc.ucsb.edu/data/chirps
	CMAP v2108 (CPC Merged Analysis of Precipitation)	Satellite + Gauge	2.5	https://psl.noaa.gov/data/gridded/data.cmap.html
	CR2 (Center for Climate and Resilience Research)	Statistical downscaling from ERA-Interim	0.05	https://www.cr2.cl/datos-productos-grillados/
	CRU v4.05 (Climate Research Unit)	Gauge-analysis	0.5	https://crudata.uea.ac.uk/cru/data/hrg/cru_ts_4.05/
	GPCC v2020 (Global Precipitation Climatology Centre)	Gauge-analysis	0.5	https://climatedataguide.ucar.edu/climate-data/gpcc-global-precipitation-climatology-centre
	GPCP v3.2 (Global Precipitation Climatology Project)	Satellite + Gauge	0.5	https://disc.gsfc.nasa.gov/datasets/GPCPMON_3.2/summary
	PERSIANN (PERSIANN-CDR)	Satellite + Artificial Neural networks	0.25	https://climatedataguide.ucar.edu/climate-data/persiann-cdr-precipitation-estimation-remotely-sensed-information-using-artificial
	University of Delaware V5.01	Gauge	0.5	http://research.jisao.washington.edu/data_sets/ud/
Temperature	CR2 v2.0 (Center for Climate and Resilience Research)	Satellite + ERA-Interim	0.05	https://www.cr2.cl/datos-productos-grillados/
	CRU v4.05 (Climate Research Unit)	Gauge-analysis	0.5	https://crudata.uea.ac.uk/cru/data/hrg/cru_ts_4.05/
	University of Delaware V5.01	Gauge	0.5	http://climate.geog.udel.edu/~climate/html_pages/download.html

$$MBE = \sum_{n=1}^{N} \left(\overline{y}_n - \overline{o}_n\right), \tag{1}$$

$$NRMSE = \sqrt{\frac{\sum_{n=1}^{N} \left(o_n - y_n\right)^2}{\sum_{n=1}^{N} {o_n}^2}}, \tag{2}$$

y_n represents the simulated data for each climatological normal, $\overline{y}$ is the mean of simulated data, o_n is the observed value of each climatological normal, $\overline{o}$ is the mean of observed data. N is the time length of the annual cycle in months.

We applied Probability Density Functions (PDFs) to evaluate the spatiotemporal distribution of monthly precipitation and temperature for all observations and models during the historical period. PDFs for each subregion were calculated by sorting all monthly grid points in space (latitude and longitude) and time (months) and partitioning these grid points into 50 bins. In Sect. 3.1.1 we present PDFs for all observations grouped by ranges of precipitation and temperature. In the Supplementary Material, Figs. S1 and S2, we include all CMIP6 individual models and their ensemble.

2.4 Model ranking

Early evidence has suggested that among the CMIP ensemble no one model is "best" for all variables and subregions (Lambert and Boer 2001). Combining results of multiple models (so-called, multi-model ensemble approach) increases the skill, reliability and forecast consistency of results compared to the solution of individual GCMs (Ge et al. 2021; Kurniadi et al. 2022). The ensemble approach also allows to quantify the uncertainty of the future climate probabilistically (Tebaldi and Knutti 2007), and uncertainties can further be reduced by selecting the best-performed models of the multi-model ensemble (MME). Yet, models composing the MME need to be carefully chosen as recent evaluations of CMIP6 GCMs have identified the 'hot model problem', resulting in a projected warming that might be larger than supported by evidence (see Hausfather et al. 2022 and references therein). The cause of projected hotter temperatures in CMIP6 is under investigation, but it might be related to an overestimated cloud feedback, among other factors (e.g., Gettelman et al. 2019). This can introduce biases in the MME toward high-temperature values (Liang et al.

Table 2 List of CMIP6 models used in the study

#	Model	Institution and Country	Resolution (lat. x lon)
1	ACCESS-CM2	Australian Community Climate and Earth System Simulator (ACCESS), Australia	1.3°×1.9°
2	ACCESS-ESM1-5	Australian Community Climate and Earth System Simulator (ACCESS), Australia	1.2°×1.9°
3	AWI-CM-1-1-MR	Alfred Wegener Institute, Helmholtz Centre for Polar and Marine Research, Germany	0.9°×0.9°
4	BCC-CSM2-MR	Beijing Climate Center, Beijing, China	1.1°×1.1°
5	CAMS-CSM1-0	Chinese Academy of Meteorological Sciences, Beijing, China	1.1°×1.1°
6	CAS-ESM2-0	Chinese Academy of Sciences, Beijing, China	1.4°×1.4°
7	CESM2-WACCM	National Center for Atmospheric Research, Boulder, USA	0.9°×1.3°
8	CIESM	Department of Earth System Science, Tsinghua University, China	1°×1°
9	CMCC-CM2-SR5	Fondazione Centro Euro-Mediterraneo sui Cambiamenti Climatici, Italy	0.9°×1.3°
10	CMCC-ESM2	Fondazione Centro Euro-Mediterraneo sui Cambiamenti Climatici, Italy	0.9°×1.3°
11	CanESM5	Canadian Centre for Climate Modelling and Analysis, Environment and Climate Change Canada, BC, Canada	2.8°×2.8°
12	E3SM-1-1	Lawrence Livermore National Laboratory, Livermore, USA	1°×1°
13	EC-Earth3	Consortium of various institutions from Spain, Italy, Denmark, Finland, Germany, Ireland, Portugal, Netherlands, Norway, the United Kingdom, Belgium, and Sweden	0.7°×0.7°
14	EC-Earth3-AerChem	Consortium of various institutions from Spain, Italy, Denmark, Finland, Germany, Ireland, Portugal, Netherlands, Norway, the United Kingdom, Belgium, and Sweden	0.7°×0.7°
15	EC-Earth3-CC	Consortium of various institutions from Spain, Italy, Denmark, Finland, Germany, Ireland, Portugal, Netherlands, Norway, the United Kingdom, Belgium, and Sweden	0.7°×0.7°
16	EC-Earth3-Veg	Consortium of various institutions from Spain, Italy, Denmark, Finland, Germany, Ireland, Portugal, Netherlands, Norway, the United Kingdom, Belgium, and Sweden	0.7°×0.7°
17	EC-Earth3-Veg-LR	Consortium of various institutions from Spain, Italy, Denmark, Finland, Germany, Ireland, Portugal, Netherlands, Norway, the United Kingdom, Belgium, and Sweden	1.1°×1.1°
18	FGOALS-f3-L	Chinese Academy of Sciences, Beijing, China	1°×1.3°
19	FGOALS-g3	Chinese Academy of Sciences, Beijing, China	2.3°×2°
20	FIO-ESM-2–0	First Institute of Oceanography, Ministry of Natural Resources (FIO), China	0.9°×1.3°
21	GFDL-CM4	National Oceanic and Atmospheric Administration, GFDL, Princeton, USA	1°×1.3°
22	GFDL-ESM4	National Oceanic and Atmospheric Administration, GFDL, Princeton, USA	1°×1.3°
23	IITM-ESM	Centre for Climate Change Research, Indian Institute of Tropical Meteorology, India	1.9°×1.9°
24	INM-CM4-8	Institute for Numerical Mathematics, Russian Academy of Science, Moscow, Russia	1.5°×2°
25	INM-CM5-0	Institute for Numerical Mathematics, Russian Academy of Science, Moscow, Russia	1.5°×2°
26	IPSL-CM5A2-INCA	Institut Pierre Simon Laplace, Paris, France	2°×2°
27	IPSL-CM6A-LR	Institut Pierre Simon Laplace, Paris, France	1.3°×2.5°
28	KACE-1–0-G	National Institute of Meteorological Sciences/Korea Meteorological Administration (NIMS-KMA), South Korea	1.9°×1.3°
29	MIROC6	Japan Agency for Marine-Earth Science and Technology, Atmosphere and Ocean Research Institute, National Institute for Environmental Studies, and RIKEN Center for Computational Science, Japan	1.4°×1.4°
30	MPI-ESM1-2-HR	Max Planck Institute for Meteorology, Germany	0.9°×0.9°
31	MPI-ESM1-2-LR	Max Planck Institute for Meteorology, Germany	1.9°×1.9°
32	MRI-ESM2-0	Meteorological Research Institute, Tsukuba, Japan	1.1°×1.1°
33	NESM3	Nanjing University of Information Science and Technology, Nanjing, China	1.9°×1.9°
34	NorESM2-LM	NorESM Climate modeling Consortium, Norway	1.9°×2.5°
35	NorESM2-MM	NorESM Climate modeling Consortium, Norway	0.9°×1.3°
36	TaiESM1	Research Center for Environmental Changes, Academia Sinica, Taiwan	0.9°×1.3°

2020). In this study, we document the late-century changes in precipitation and temperature of GCMs identifying the 'hot models', i.e. those models showing equilibrium climate sensitivity (ECS) values above the IPCC AR5 likely range of 1.5–4.5 °C (Scafetta 2022; Tokarska et al. 2020). However, we do not discard these models in our analysis and present all available projections. We ranked all GCMs performance in space and time using the pattern correlation coefficient (PCC) and the Taylor skill score (TSS, Taylor 2001), respectively. PCC (centered) measures the similarity

of two variables. It is computed as the Pearson correlation applied to each pair of grid points of the simulated and observed fields to show how well the observed spatial pattern is captured by simulations (Rivera and Arnould 2020; Shiferaw et al. 2018). TSS ranks GCMs based on how well they replicate the annual cycle of observed fields and has been successfully applied to account for GCMs skill in a variety of studies (Guo et al. 2021; Lun et al. 2021; Ngoma et al. 2021; Xin et al. 2020). The equations to calculate PCC and TSS are given as follows:

$$\mathrm{PCC} = \frac{\sum_{m=1}^{M}\left(y_m - \overline{y}\right)\left(o_m - -\overline{o}\right)}{\left[\sum_{m=1}^{M}\left(y_m - \overline{y}\right)^2 \sum_{m=1}^{M}\left(o_m - \overline{o}\right)^2\right]^{\frac{1}{2}}}, \tag{3}$$

where y_m and o_m are the simulated and observed data at the mth grid point, respectively. $\overline{y}$ and $\overline{o}$ represent the mean value of simulated and observed data across M total of grid points.

$$TSS = \frac{4\left(1 + R_m\right)^2}{\left(\frac{\sigma_m}{\sigma_o} + \frac{\sigma_o}{\sigma_m}\right)^2\left(1 + R_0\right)^2}, \tag{4}$$

where R_m is the correlation of the annual cycle for the reference period between each GCM and the observation ensemble, σ_m and σ_o are the standard deviations of simulated and observed patterns of the annual cycle, respectively. R_0 is the maximum correlation attainable, set as 0.999. TSS approaches unity as the model spatial variance is closer to the observed variance, and R_m approximates R_0.

After selecting the top 5 models from both PCC and TSS ranking list for each subregion, the final model ranking was done, identifying the 'hot models' informed by Tokarska et al. (2020) and Scafetta (2022). We finally plotted annual mean precipitation change against temperature change of the late-century period (2080–2099) relative to the reference period (1986–2014). This gave us a set of models that are closer to observations, unbiased towards warming, and represent enough ranges of uncertainties in future climate changes.

3 Results and discussion

3.1 Annual cycle

3.1.1 Current climate from the observation ensemble

Figure 2 shows the spatially averaged annual precipitation cycle for all models and the observation ensemble. Observations illustrate the aridity gradient with decreasing latitude in continental Chile. The arid Northern Chile subregion receives a median precipitation of 0.16 (Inter-Quartile range, IQR = 0.18) mm/day, most of which falling in the months of December, January, and February, with amounts greater than 0.33 mm/day (75th percentile of the annual cycle). Further south, winter precipitation dominates the annual cycle of Central Chile and Northern Patagonia, where the months of May, June, and July make the largest contribution to the annual precipitation. However, the magnitude of precipitation is greater in Northern Patagonia, which receives about three times more precipitation than its northern neighbor [2.67 (IQR = 1.73) vs. 0.91 (IQR = 1.39) mm/day]. In Southern Patagonia, precipitation abounds all year around, with a median of 2.79 (IQR = 0.25) mm/day. Here, maximum precipitation occurs during March, April, and May, which receive more than the 75th percentile (2.91 mm/day) of precipitation during the annual cycle (Fig. 2d).

Figure 3 evidences that the annual mean temperature ranges from 11.32 °C in Northern Chile to 6.23 °C in Southern Patagonia. During December, January, and February, when the increased insolation in summer warms the land in all subregions, mean temperature varies from 14.26 °C in Northern Chile to 9.57 °C in Southern Patagonia. Northern Chile exhibits slightly lower temperatures in the austral summer than Central Chile (− 1.67 °C), which may be due to much the higher mean elevation of this region (Fig. 1). Besides the more poleward position of Northern and Southern Patagonia with respect to northern and Central Chile, lower temperature over this region is also influenced by the summer increase in onshore moisture transport described by Garreaud et al. (2013), which advent cool air over land. During the winter months, the mean temperature varies from 7.95 to 2.16 °C between the Northernmost and the southernmost regions. As illustrated in Fig. 7, while observations indicate an absence of a west–east gradient for temperature in Patagonia, there is a pronounced meridional asymmetry in precipitation, with peak values occurring in the western side of Southern Patagonia. Here, a band of maximum annual precipitation stretches between parallel 47°S and 55°S and between meridians 72.5°W and 77°W. Precipitation rapidly decreases towards the east to a minimum of 0.57 mm/day in Tierra del Fuego.

To evaluate the dispersion between the observations over each subregion we used Probability Density Functions (PDFs). These are presented as density boxplots for a set of ranges of precipitation and temperature in Figs. 4 and 5, respectively (original PDFs can be seen in the Supplementary Material). We detected substantial differences among observations in the distribution of precipitation in the wetter subregions of Northern and Southern Patagonia. The frequency density of the months with low precipitation (≤ 2 mm/day) is much greater in CMAP than in the other products. PERSIANN exhibits the highest frequency of months with 2–4 mm/day for the same subregions and in

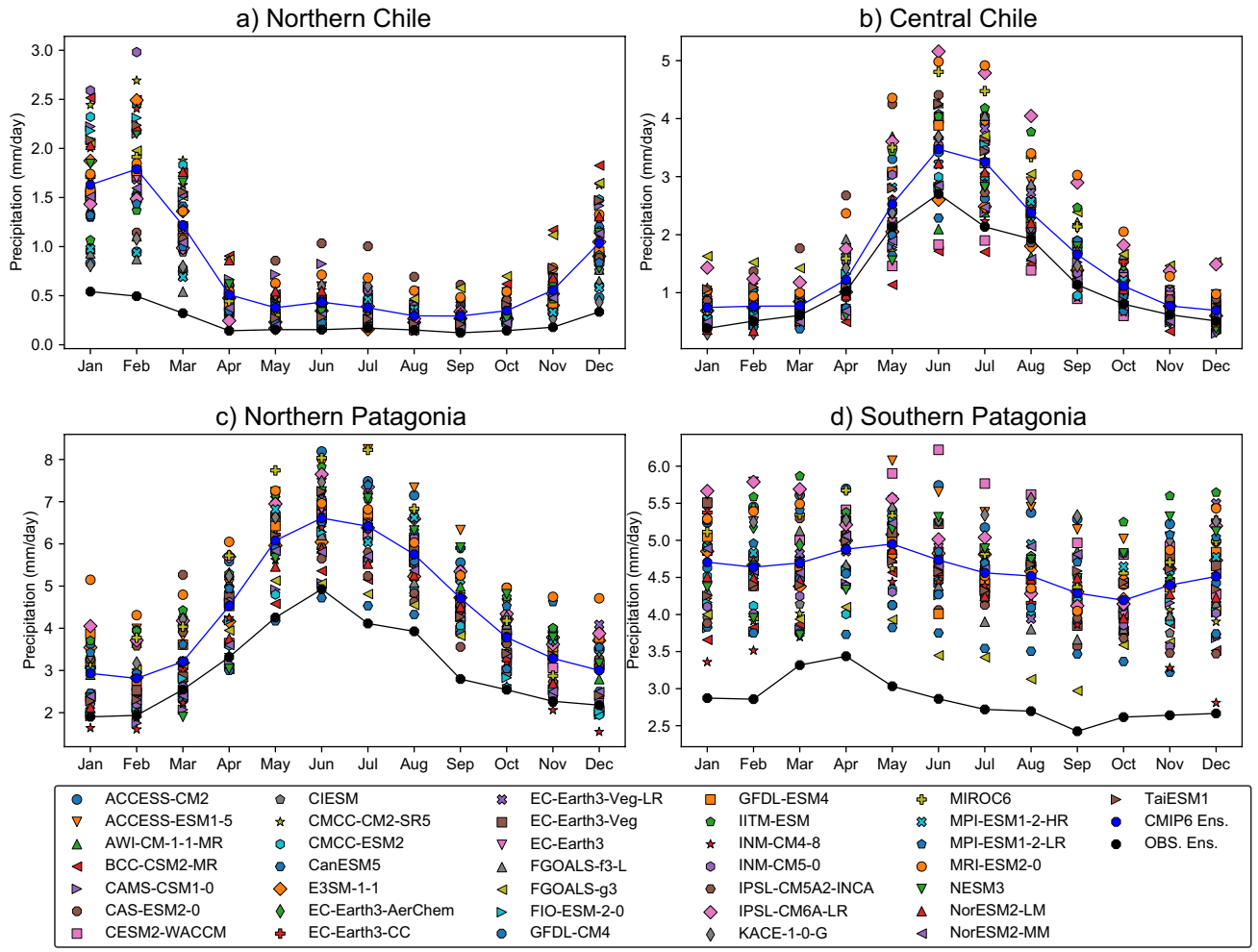

Fig. 2 Annual precipitation cycle in CMIP6 models and the observation ensemble dataset for Chile. Each point in the plot is the monthly average of the dataset across the reference period (1986–2014) and averaged across each subregion. Blue and black lines show the annual cycle of the CMIP6 ensemble (CMIP6 Ens.) and Observation Ensemble (Obs. Ens.), respectively

Southern Patagonia it also shows the highest frequency for months with intensity ≥ 4 mm/day (Fig. 4b, c). CMAP and PERSIANN are the datasets showing the highest frequency of low-intensity months (≤ 2 mm/day) for Central Chile, although in general, the observations are relatively more homogeneous in the representation of low and medium-intensity precipitation months in this semi-arid region than in Patagonia (Fig. 4b). In Northern Chile, where the monthly precipitation amount rarely exceeds 2 mm/day, CHIRPS and CMAP showed the greatest frequency and greatest IQR of the months with low intensity (< 2 mm/day).

The monthly distribution of temperature presents more agreement among observations than the precipitation in all regions (Fig. 5). In the two northernmost regions the UDelaware dataset shows the greatest frequency for the months with lowest temperatures (< 5 °C) and the smallest frequency for the rest of the months with respect to the other two datasets. Torrez-Rodriguez et al. (2023) showed that CR2 is substantially warmer than CRU and UDelaware over high mountains between 25 and 35°S dataset. Our results suggest that the CR2 dataset exhibits the highest frequency of the temperature values in the range of 10–15 °C (Fig. 5a), but in terms of the PDF shape the CR2 is very similar to the CRU in all subregions (Fig. S2).

3.1.2 CMIP6 ensemble *versus* observations

In Fig. 6, we summarize the results of subregional differences in the annual cycle between CMIP6 models and the observation ensemble for the period 1986–2014 using the difference in annual Fourier harmonic amplitude (Fig. 6a), the difference in the climatological peak month (Fig. 6b), MBE (Fig. 6c), and NRMSE (Fig. 6d). The corresponding values for each individual model are provided in Supplementary Material (Tables S1 and S2). First, we verified that the annual Fourier harmonic was able to successfully capture

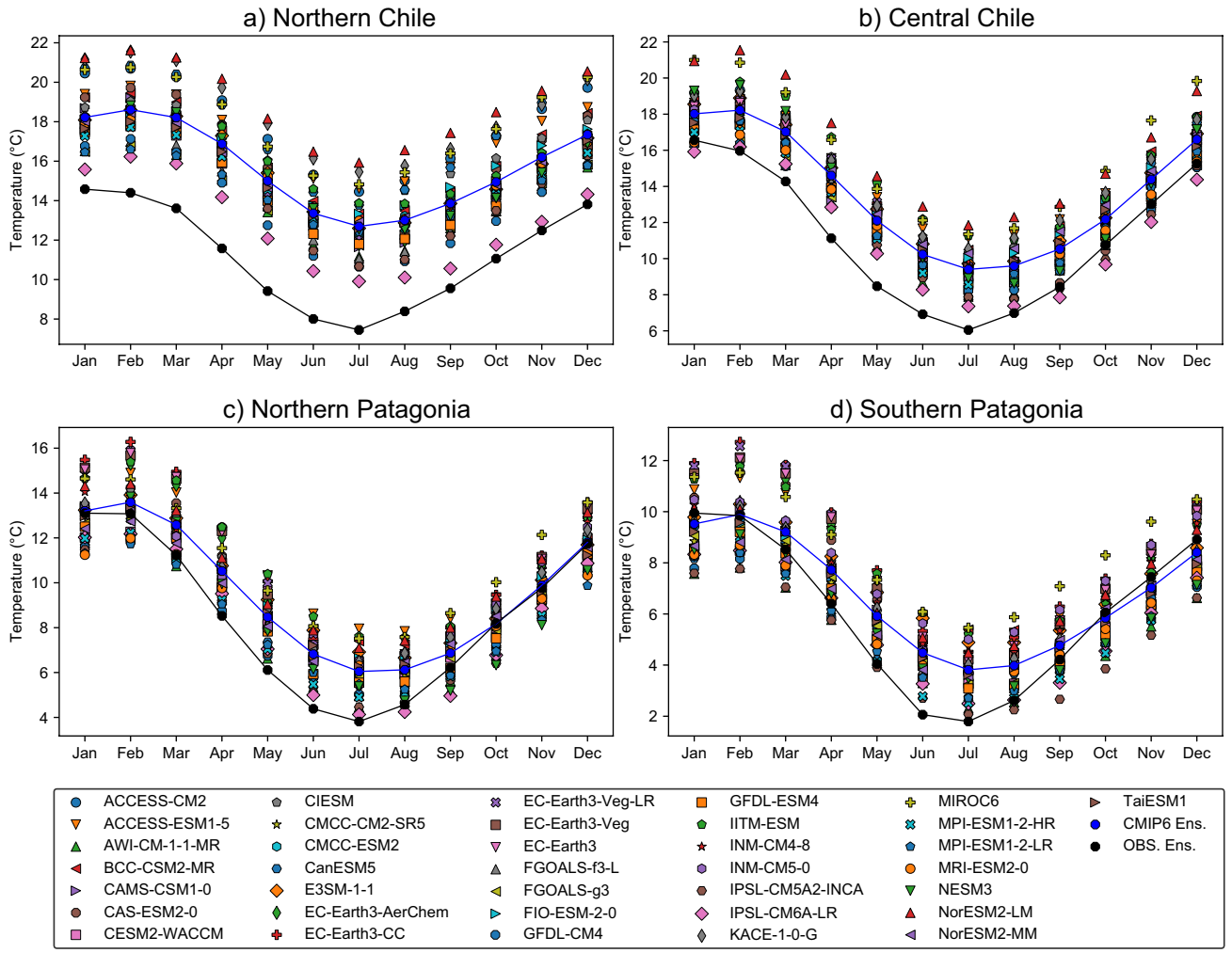

Fig. 3 Annual cycle of temperature in CMIP6 models and observation ensemble dataset for Chile. Each point in the plot is the monthly average of the dataset across the reference period (1986–2014) and averaged across each subregion. Blue and black lines show the annual cycle of the CMIP6 ensemble (CMIP6 Ens.) and Observation Ensemble (OBS. Ens.), respectively

the observed annual cycle of precipitation and temperature. In case of precipitation, over the most of Chile the corresponding explained variance is greater than 90% (Fig. S3). A relatively low explained variance (less than 65%) over a part of Northern Chile and Southern Patagonia is likely due to weak amplitude of the observed annual cycle (Fig. 2a, d). For temperature, the annual Fourier harmonic explains more than 98% of the annual cycle over the entire Chile (Fig. S4). These results give us reliable amplitude and phase to evaluate the performance of CMIP6 models for the analysis of the annual cycle.

Figure 6a evidences a general overestimation (underestimation) of the amplitude of annual cycle of precipitation (temperature). In Northern Chile, CMIP6 showed the greatest median difference in the precipitation amplitude (325% or 0.71 mm/day), followed by Southern Patagonia (63% or 0.16 mm/day), Northern Patagonia (49% or 0.61 mm/day) and Central Chile (19% or 0.17 mm/day,). Temperature amplitude differences revealed differences for all subregions that ranged from − 0.8 °C in Northern Chile to − 1.4 °C in Southern Patagonia. Figure 6b shows that the timing of the climatological peak month for precipitation is generally delayed by up to 21 days in Central Chile, 10 days in Northern Patagonia, 8 days in Southern Patagonia, and 3 days in Northern Chile. However, Central Chile and Southern Patagonia showed a high inter-model variability, with an IQR of 27 days and 74 days, respectively. The models exhibited a delay also in the annual temperature cycle, with a range of 10–15 days across the regions. The interquartile range (IQR) was less than 6 days, indicating a weak inter-model variability.

The magnitude of the average model bias is shown by the mean bias error (MBE). This metric, however, needs to be interpreted alongside NRMSE, given that the total

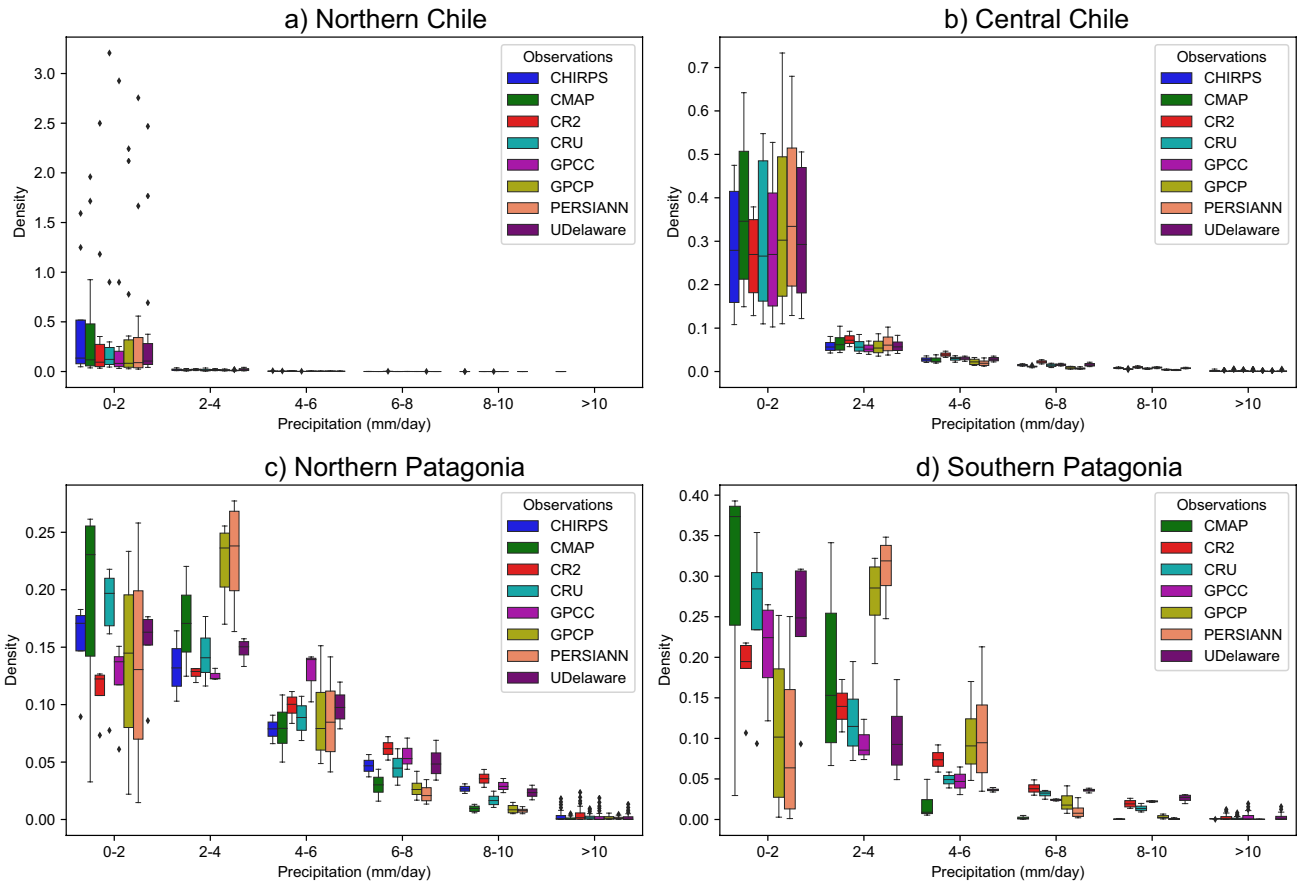

Fig. 4 Probability density functions (PDFs) of monthly precipitation for specific intensity ranges over four subregions of Chile. To construct the PDFs in each subregion, we separated all monthly precipitation over each latitude and longitude grid cell using 50 bins (see original PDFs in Supplementary Material)

precipitation amount varies significantly among the different subregions. The second lowest MBE occurs in Northern Chile (extremely arid) with a median of 0.44 mm/day. However, this subregion shows the greatest relative error as shown by the NRMSE with a value of 2.17 (205%). Central Chile presented the lowest NRMSE of 0.44 (37%), followed by Northern Patagonia with 0.46 (42%). Southern Patagonia showed the greatest MBE of 1.66 mm/day and the second largest NRMSE of 0.66 (65%). Northern and Central Chile presented the highest MBE with 2.6 °C and 2.1 °C, respectively. This error decreases with latitude down to 0.6 °C in Southern Patagonia. However, projections of GCMs are highly variable as shown by an IQR of 1.57 °C (Fig. 3). NRMSE registered values less or equal to 0.2 °C across subregions.

3.2 Spatial pattern of annual means: CMIP6 ensemble bias

The spatial bias of the annual mean for precipitation and temperature of the CMIP6 ensemble is portrayed in Figs. 7 and 8, respectively. CMIP6 precipitation shows a strong wet bias reaching up to 6.8 mm/day in Southern Patagonia and up to 5.8 mm/day in the southern tip of Northern Patagonia. A wet bias is present in Northern Chile, which shows a maximum of 4.5 mm/day towards the high Andean Plateau in Bolivia. Central Chile registered the lowest precipitation bias for Chile with values less than 1 mm/day. Central Chile is the subregion where CMIP6 best performs, as it shows the best spatial and temporal fit with respect to the observations (Fig. 9). This result, though, does not extend to near-surface temperature as it shows the second largest positive bias with 7 °C in high-elevation areas of the Andes Mountains, certainly due to an unresolved topography by coarse-resolutions CMIP6 models. This bias is only surpassed by 8 °C in specific areas in the Atacama Desert in Northern Chile. In the remaining subregions, temperature bias ranges within ± 2 °C, except for a slight cool bias at about 47°S (Fig. 8). Figure 9 exhibits the latitudinal averages of temperature and precipitation of the CMIP6 and observational ensembles. This figure displays the strong bias in precipitation from parallel 43S (Northern Patagonia) with a

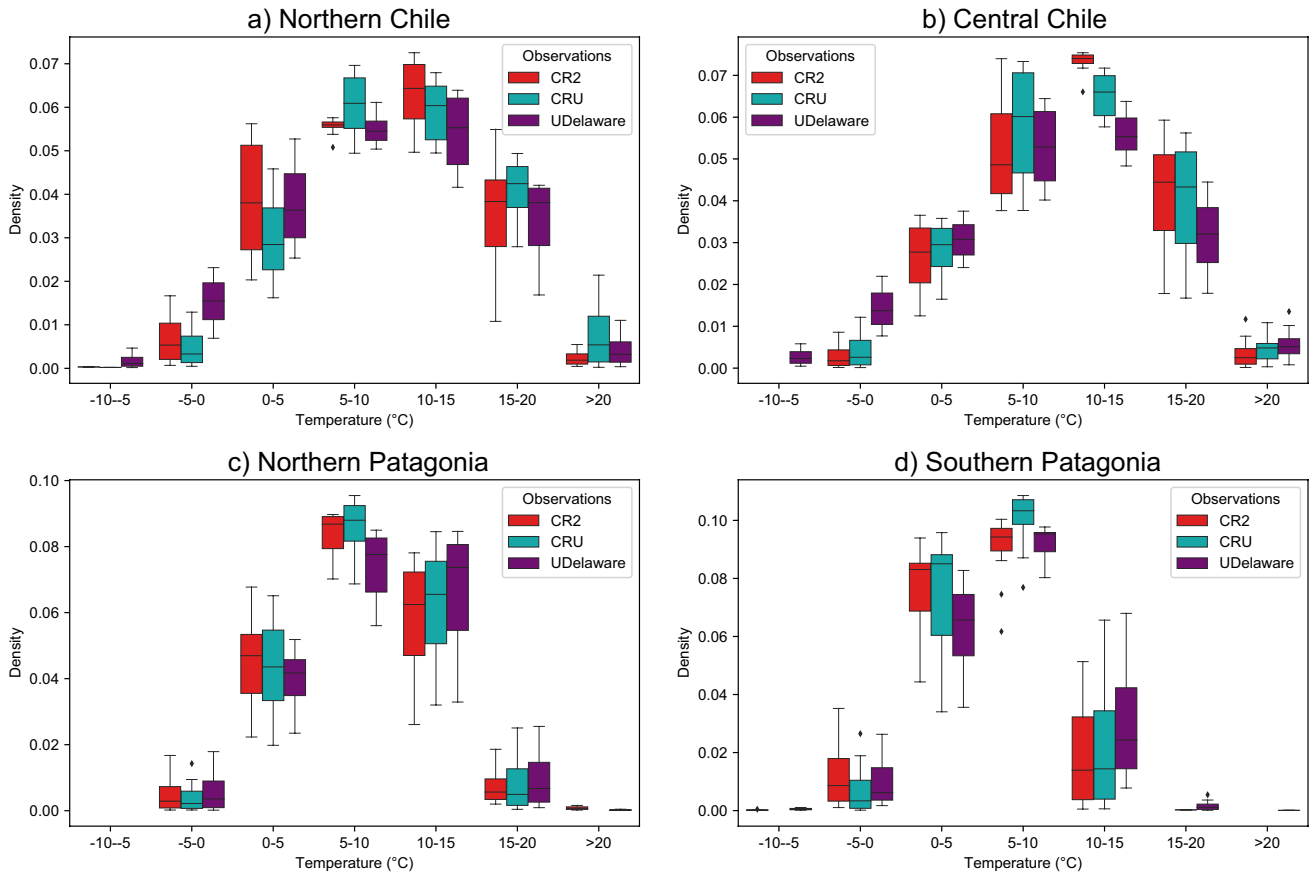

Fig. 5 Same as Fig. 4 but for monthly temperature (see original PDFs Supplementary Material)

maximum bias around parallel 49S (Southern Patagonia). It reveals the great difficulty of CMIP6 models in replicating the spatial pattern of precipitation in Patagonia. This region is characterized by a reduced network of ground observations in space and time which impose challenges in validating climate models. For temperature, the strongest bias is found in Northern Chile with a maximum at around parallel 30S along the Andes. Figure 9 also replicates the proportional change in temperature according to the climate change scenario, with warming that increases from scenario SSP126 towards scenario SSP585.

We used the pattern correlation coefficient (PCC) to evaluate the subregional spatial agreement between CMIP6 models and the observation ensemble over the annual mean of precipitation and temperature across the reference period (1986–2014). Results are shown in Table 3 as the PCC average of precipitation and temperature for individual models. Overall, Northern Chile showed the largest PCC across all subregions with a median of 0.89 (IQR = 0.06). Here, 30 out of 36 models (83%) scored PCC > 0.8, suggesting that CMIP6 simulations perform well in replicating the observed spatial pattern of precipitation and temperature. On the other hand, Southern Patagonia presented the lowest PCC of all subregions with a median of 0.65 (IQR = 0.11). Only 1 out of 36 CMIP6 models in this subregion scored a PCC > 0.8 (Table 3). This result was triggered by a wet bias of more than 6 mm/day near coastal areas (Fig. 7). Northern Patagonia showed a median score of 0.81 (0.04), and 18 out of 36 models (50%) had a PCC > 0.8. Central Chile's median PCC was 0.78 (0.16), and 13 out of 36 models (36%) scored a PCC > 0.8. Since Central Chile's precipitation bias was low, this score is attributable to the unsatisfactory simulation of the annual spatial mean of temperature in the northern extreme of this subregion (Fig. 8c). For the entirety of Chile, 35 out of 36 models showed PCC > 0.8, and the best-performing models on PCC scores were: GFDL-CM4, GFDL-ESM4, EC-Earth3-Veg-LR, FGOALS-f3-L, and EC-Earth3-CC. Grouped by model family, GFDL and EC-EARTH3 best described the spatial pattern of precipitation and temperature. These results compare to the study of Rivera and Arnauld (2020), who evaluated precipitation projections of 14 CMIP6 models for a region covering Central Chile and Northern Patagonia in our research. Though the study of Rivera and Arnauld (2020) is not directly comparable with our study (they analyzed simulations of precipitation only over the longest period, 1901–2014), they applied a similar

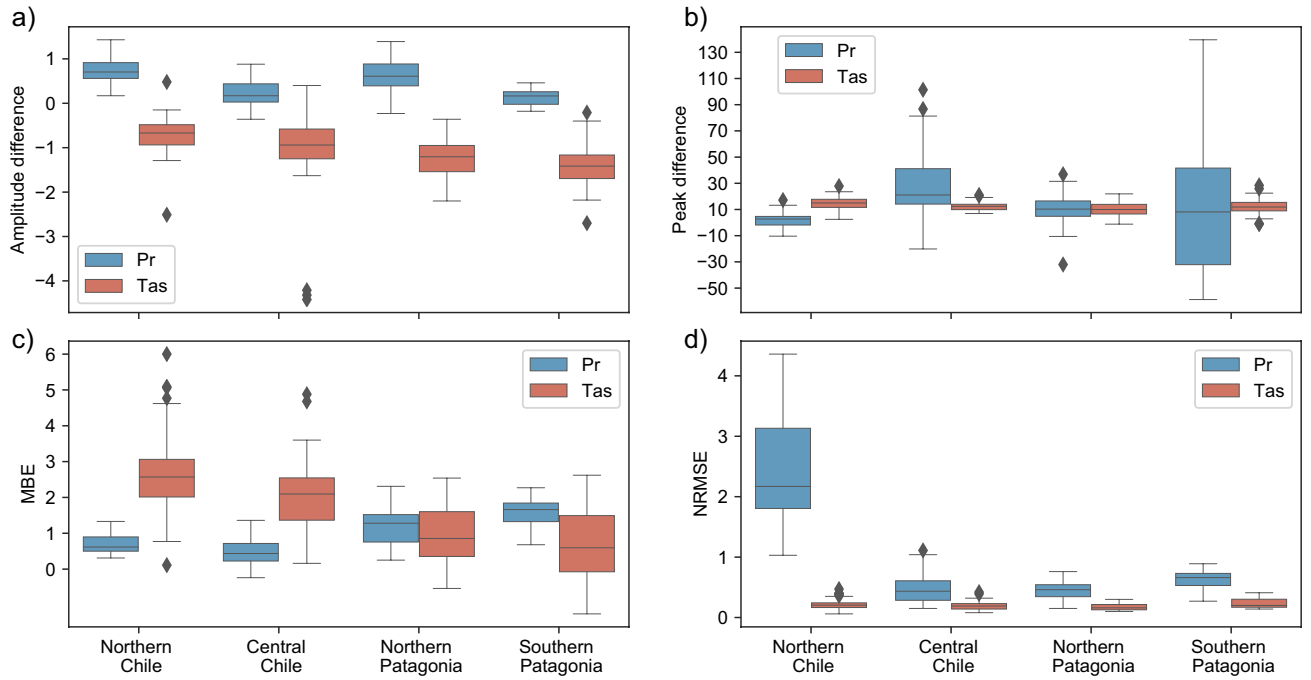

Fig. 6 Summary of metrics used to validate the annual cycle of CMIP6 models against the observations for the four subregions for the period 1986–2014: **a** amplitude difference, **b** peak month difference, **c** MBE and **d** NRSME. Amplitude difference and MBE for Precipitation (Pr) is in mm/day, while for temperature (Tas) it is in °C. Peak difference is in days and NRMSE values are dimensionless

methodology to evaluate the spatial pattern of CMIP6 projections. As in our study, Rivera and Arnauld (2020) found that most models scored a PCC > 0.8 with a marked overestimation of precipitation.

3.3 Model ranking of annual cycle

So far, we have thoroughly evaluated the spatiotemporal performance of CMIP6 models across Chile. We finally summarized the models' performance by applying the Taylor Skill Score metric (TSS) over the annual cycle, which helped us to select the best-performing models for precipitation and temperature. TSS results are displayed in Table 4, with the five best-performing models shown in bold for each of the four subregions and for the entire Chile. Although models replicated the precipitation pattern in Northern Chile, they all strongly overestimated this variable during the rainy season (December, January, and February). This bias is represented on the TSS metric, which, averaged across models, was lowest among all subregions, including the entire Chile (0.63). Those models with the best performance in describing the average annual precipitation cycle and temperature were: CAS-ESM2-0, FGOALS-f3-L, ACCESS-CM2, KACE-1-0-G, and MPI-ESM1-2-HR. The model ACCESS-CM2 is identified as a 'hot model' by Tokarska et al. (2020) and Scafetta (2022). The bias of these warm models is discussed in Sect. 3.4.

Central Chile scored the highest average TSS across all subregions (0.90). The best-performing models were: CanESM5, INM-CM4-8, CAMS-CSM1-0, IPSL-CM5A2-INCA, and MPI-ESM1-2-HR. It is worth noting that CanESM5 had the highest score among all CMIP6 models for Central Chile. This model was also identified as the best performing in the study of Rivera and Arnould (2020). However, it is a "hot model" and, as it will be shown in Sect. 3.4, presents the warmest temperature projection for the end of the century. Therefore, care should be taken when considering this model for future temperature predictions in Central Chile. Another interesting feature of Central Chile is that the model ensemble scored the sixth-best TSS score for the subregion (0.95).

Northern Patagonia scored Chile's second-highest average TSS metric (0.87). The best-performing models were: GFDL-CM4, FGOALS-f3-L, EC-Earth3-CC, EC-Earth3, and IPSL-CM5A2-INCA. In Southern Patagonia, the ensemble mean had the highest TSS (0.84), and the best-performing models were: FGOALS-f3-L, MIROC6, NorESM2-LM, FGOALS-g3, and MPI-ESM1-2-HR. The best-performing models for Chile were: AWI-CM-1-1-MR, NorESM2-LM, MPI-ESM1-2-HR, IPSL-CM5A2-INCA, and IITM-ESM.

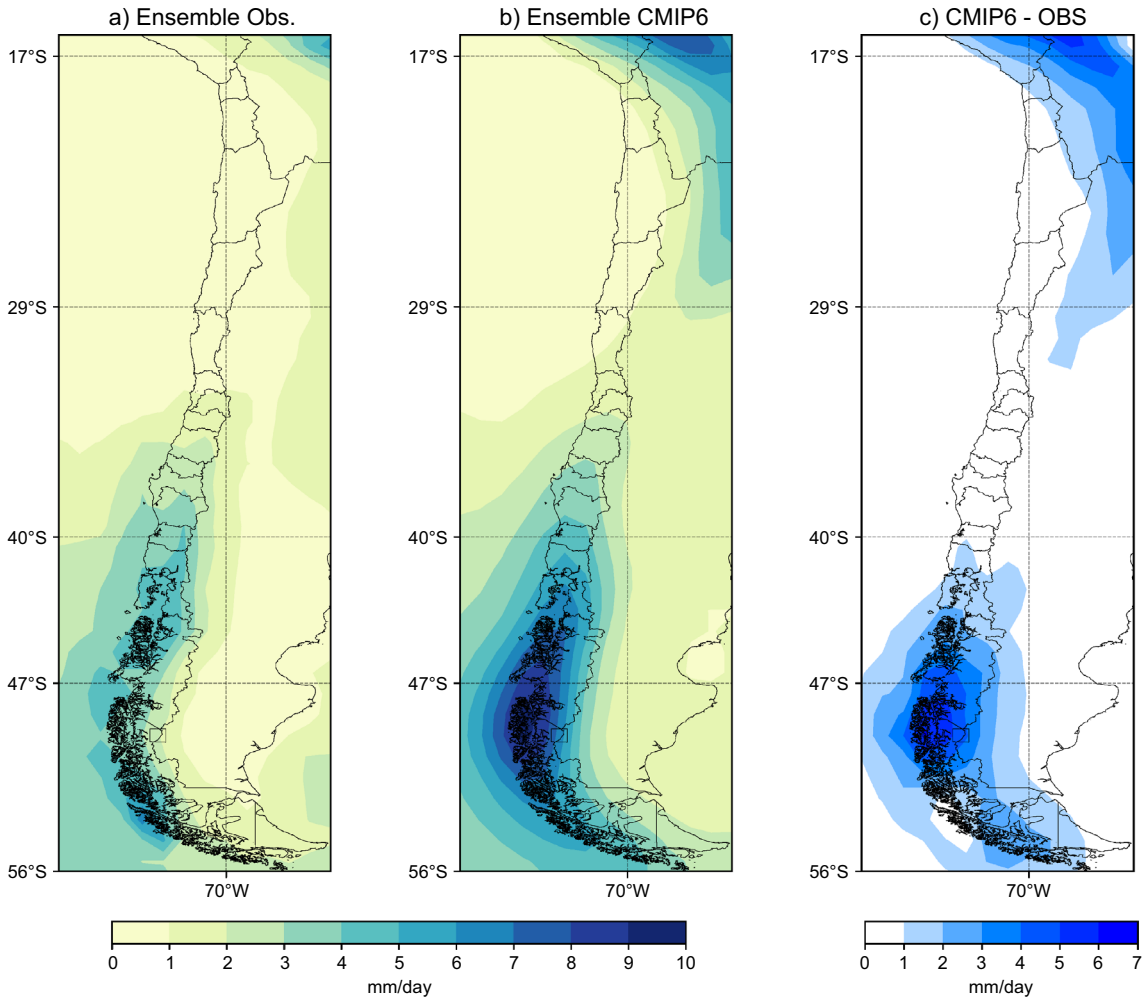

Fig. 7 Spatial patterns of the annual mean precipitations for the period 1986–2014: **a** displays the ensemble mean of the 8 observational datasets, **b** shows the ensemble mean of 36 CMIP6 models, and **c** shows the CMIP6 mean bias (values ± 1 are shown in white). Units for all maps are in mm/day. Note that the Y-axis shows the latitudinal limits of each subregion considered in this study (Fig. 1)

3.4 Future projections (2080–2099)

In this section, we analyze the changes in temperature and precipitation at the end of the century with respect to the historical period under four emission scenarios (Figs. 10 and 11, respectively). The precipitation changes are spatially consistent between CMIP6 models in Central Chile and Northern Patagonia and become robust (at least 90% of models agree on the sign of precipitation change) from scenario SSP245 onwards, which shows a precipitation reduction of 10–20% (Fig. 10). This reduction is much more substantial when increasing the strength of the anthropogenic radiative forcing. In Central Chile, under scenario SSP585, CMIP6 models project a mean reduction of 30–40% of annual precipitation that is spatially consistent across 90% of CMIP6 GCMs. Similarly to Almazroui et al. (2021), we found that the changes tend to become stronger with increasing radiative forcing, suggesting a potentially simple proportional scaling. There is less inter-model agreement in the projected precipitation change in the extremely dry and wet subregions. In Northern Chile, the CMIP6 ensemble forecasts up to a 20% decrease in mean annual precipitation. However, this tendency is inconsistent across GCMs (non-robust change) as well as across the scenarios as a decrease is projected under scenarios SSP126, SSP245 and SSP370, and a general non-robust increase in precipitation under scenario SSP585 (Fig. 10). The robust drying projected for the Central Chile and Northern Patagonia extends to the northern part of Southern Patagonia in scenarios SSP370 and SSP585, reaching up to 20% at around parallel 47°S. In the southernmost portion of the latter subregion, the sign of the changes varies amongst GCMs (see Fig. 12) showing a non-robust increase in the ensemble mean.

Our findings are in agreement with previous studies focused on the future climate change in Chile in CMIP5 and CMIP6. For instance, Bozkurt et al. (2018) reported

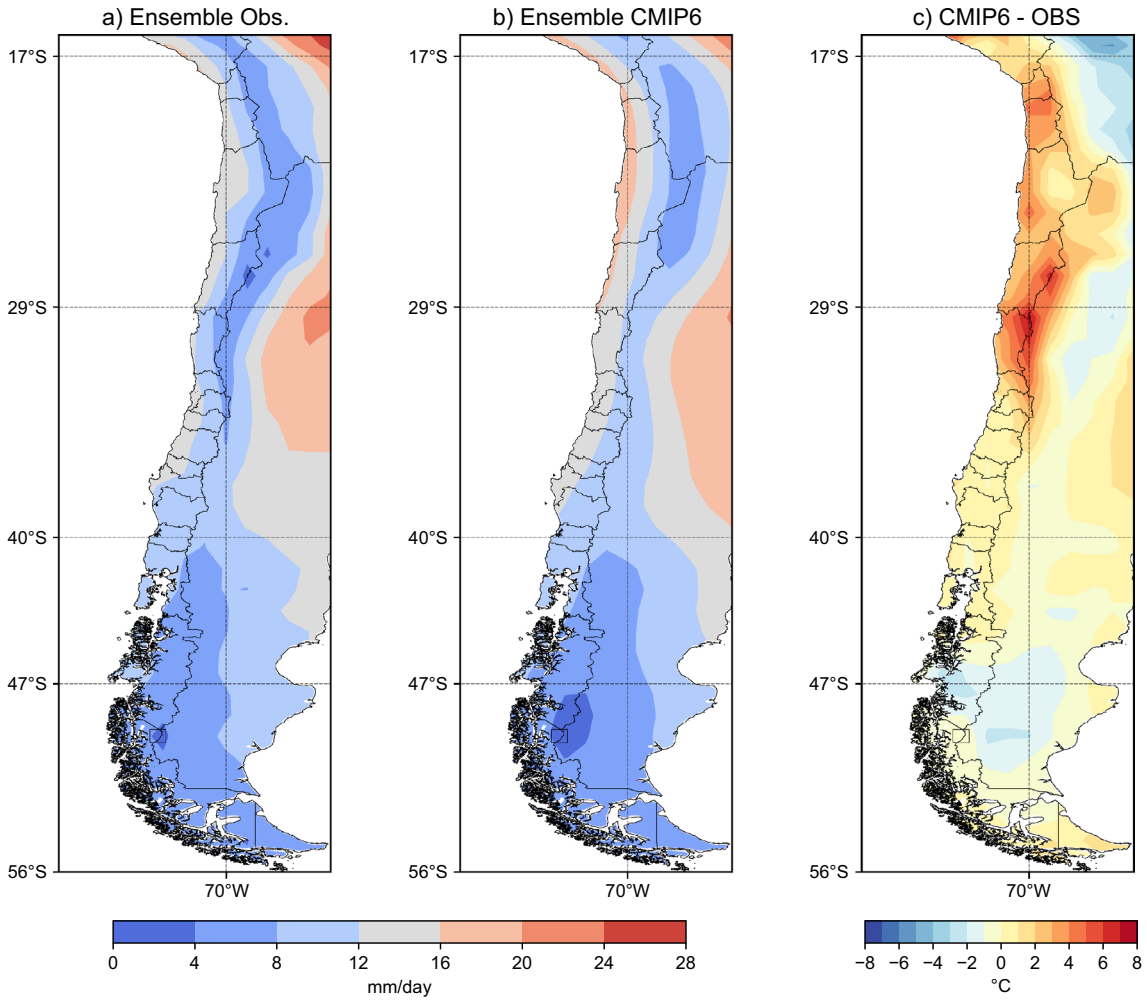

Fig. 8 Spatial patterns of the annual mean temperature for the period 1986–2014: **a** displays the ensemble mean of the 3 observational datasets, **b** shows the ensemble mean of 36 CMIP6 models, and **c** shows the CMIP6 mean bias. Units for all maps are in °C. Note that the Y-axis shows the latitudinal limits of each subregion considered in this study (Fig. 1)

a drying of up to ~ 30% over Central Chile using projections from CMIP5 by the end of the century. The trends identified in CMIP5 are consistent with recent CMIP6 models that project a robust drying over Mediterranean-type climate regions, including Central Chile (Cook et al. 2020). When compared with the historical period, future changes in precipitation over Central Chile are more significant than the baseline variability under scenarios SSP370 and SSP585, and changes in precipitation become temporarily and spatially robust from mid-century onwards, reaching − 2 mm/day compared to the historical period (Almazroui et al. 2021). CMIP6 projected changes in precipitation, especially in Central Chile and Northern Patagonia, are related to a change in the width and strength of the Hadley cell with a poleward storm-track shift. This implies a southern expansion of the band of subtropical subsidence, leading to enhanced mid-latitude tropospheric warming and poleward shifts of the subtropical dry zone and increased subtropical drought events documented since 1979 (Hu et al. 2011; Huang et al. 2016). This change in general circulation features is replicated by CMIP6 models, which show a total annual-mean trend in the width of the Hadley cells of $0.13° \pm 0.02°$ per decade over 1970–2014 across historical simulations (Xia et al. 2020) and that is 2–3 times larger in the Southern Hemisphere (SH) (Grise and Davis 2020). It's been suggested that natural SST variability primarily related to El Niño Southern Oscillation (ENSO) and the Pacific Decadal Oscillation (PDO) are the main factors explaining the observed shift patterns (Allen and Kovilakam 2017). PDO also contributes about half of the observed precipitation trend in Central Chile (Boisier et al. 2016), which is expected to be reinforced in the future by anthropogenic forcing. By consequence, Central Chile will experience the strongest increments in meteorological droughts by the end of the century with

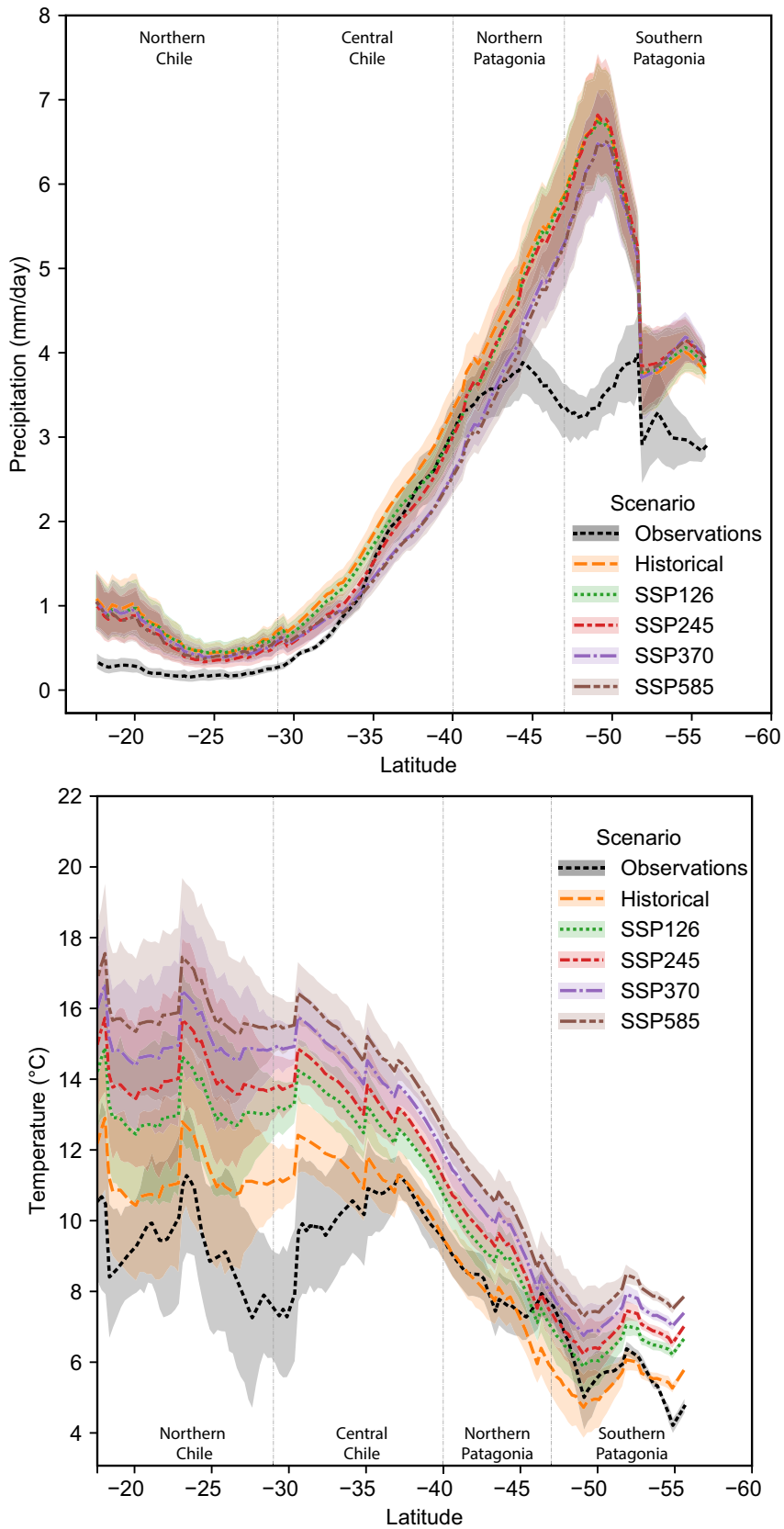

Fig. 9 Mean annual precipitation and temperature versus latitude across Chile. Vertical grey dashed lines show the latitudinal limits of each subregion. Values are averaged across longitude and show the latitudinal variations for the observation ensemble for the period 1986–2014 (Observations), CMIP6 historical ensemble for the period 1986–2014 (Historical), and projections for four emission scenarios (SSP126, SSP245, SSP370, and SSP585) for the period 2080–2099. Shaded areas around lines represent the 95% confidence interval around the mean of latitude grid points

Table 3 PCC ranking summary of CMIP6 models for Chile

Model	N. CHL	C. CHL	N. Pat	S. Pat	Chile
ACCESS-CM2[a]	0.840	0.679	0.819	0.631	0.865
ACCESS-ESM1-5	0.800	0.660	**0.838**	0.739	0.890
AWI-CM-1-1-MR	0.839	**0.883**	0.810	0.646	0.881
BCC-CSM2-MR	0.846	0.734	0.790	0.659	0.821
CAMS-CSM1-0	0.873	0.844	0.796	0.599	0.867
CAS-ESM2-0	0.895	0.747	0.567	0.444	0.797
CESM2-WACCM[a]	0.912	0.765	0.776	**0.746**	0.861
CIESM[a]	**0.920**	0.789	0.802	0.721	0.889
CMCC-CM2-SR5	0.902	0.653	0.810	0.713	0.842
CMCC-ESM2	0.904	0.697	0.820	0.701	0.853
CanESM5[a]	0.774	0.742	0.720	0.547	0.826
E3SM-1-1[a]	0.894	0.831	0.774	0.669	0.892
EC-Earth3-AerChem	0.896	**0.877**	**0.842**	0.602	0.892
EC-Earth3-CC	0.894	0.866	**0.843**	0.618	**0.893**
EC-Earth3-Veg-LR	0.891	0.852	**0.847**	0.633	**0.902**
EC-Earth3-Veg	0.894	0.871	**0.841**	0.616	0.893
EC-Earth3	0.891	0.869	0.838	0.612	0.890
FGOALS-f3-L	**0.917**	0.856	0.757	0.556	**0.895**
FGOALS-g3	0.891	0.800	0.780	0.668	0.846
FIO-ESM-2–0	0.914	0.769	0.817	**0.743**	0.877
GFDL-CM4	**0.947**	**0.905**	0.829	0.649	**0.923**
GFDL-ESM4	**0.943**	**0.903**	0.800	0.647	**0.917**
IITM-ESM	0.849	0.781	0.793	0.554	0.888
INM-CM4-8	0.785	0.582	0.767	**0.746**	0.863
INM-CM5-0	0.787	0.600	0.786	0.734	0.866
IPSL-CM5A2-INCA	0.848	0.469	0.508	0.634	0.841
IPSL-CM6A-LR[a]	0.878	0.781	0.740	0.601	0.873
KACE-1–0-G	0.783	0.682	0.733	0.595	0.846
MIROC6	0.857	0.419	0.827	0.722	0.850
MPI-ESM1-2-HR	0.875	**0.876**	0.824	0.609	0.893
MPI-ESM1-2-LR	0.843	0.726	0.817	0.631	0.882
MRI-ESM2-0	**0.938**	0.839	0.805	0.604	0.890
NESM3[a]	0.856	0.701	0.810	0.664	0.868
NorESM2-LM	0.718	0.587	0.744	**0.806**	0.815
NorESM2-MM	0.881	0.787	0.819	**0.745**	0.881
TaiESM1	0.911	0.780	0.808	0.689	0.870

Values show the regional average of PCC for precipitation and temperature compared against the ensemble of observations from 1986 to 2014. Bold values show the five best-performed models for Northern Chile (N. CHL), Central Chile (C. CHL), Northern Patagonia (N. Pat), Southern Patagonia (S. Pat), and the entire domain (Chile)

[a]Models with ECS values above the IPCC AR5 likely range (1.5–4.5 °C). 'Hot models' were identified from Tokarska et al. (2020) and Scafetta (2022)

Table 4 TSS ranking summary of CMIP6 models for Chile

Model	N. CHL	C. CHL	N. Pat	S. Pat	Chile
ACCESS-CM2[a]	**0.811**	0.865	0.833	0.771	0.816
ACCESS-ESM1-5	0.571	0.885	0.775	0.715	0.761
AWI-CM-1-1-MR	0.762	0.937	0.904	0.767	**0.919**
BCC-CSM2-MR	0.551	0.876	0.862	0.411	0.603
CAMS-CSM1-0	0.571	**0.967**	0.825	0.533	0.842
CAS-ESM2-0	**0.864**	0.837	0.88	0.778	0.809
CESM2-WACCM[a]	0.615	0.847	0.811	0.568	0.863
CIESM[a]	0.618	0.842	0.788	0.661	0.756
CMCC-CM2-SR5	0.53	0.826	0.894	0.639	0.642
CMCC-ESM2	0.521	0.871	0.869	0.573	0.625
CanESM5[a]	0.56	**0.979**	0.915	0.71	0.648
E3SM-1-1[a]	0.559	**0.956**	0.893	0.692	0.702
EC-Earth3	0.652	0.925	**0.922**	0.663	0.81
EC-Earth3-AerChem	0.669	0.923	0.901	0.726	0.833
EC-Earth3-CC	0.633	0.921	**0.923**	0.684	0.844
EC-Earth3-Veg	0.646	0.924	0.896	0.702	0.85
EC-Earth3-Veg-LR	0.625	0.891	0.867	0.642	0.82
FGOALS-f3-L	**0.855**	0.836	**0.935**	**0.832**	0.866
FGOALS-g3	0.515	0.935	0.921	**0.792**	0.607
FIO-ESM-2–0	0.521	0.88	0.833	0.774	0.753
GFDL-CM4	0.625	0.948	**0.939**	0.748	0.823
GFDL-ESM4	0.605	0.91	0.91	0.76	0.831
IITM-ESM	0.582	0.779	0.896	0.684	**0.872**
INM-CM4-8	0.604	**0.975**	0.811	0.616	0.831
INM-CM5-0	0.572	0.91	0.813	0.61	0.779
IPSL-CM5A2-INCA	0.72	**0.956**	**0.921**	0.708	**0.884**
IPSL-CM6A-LR[a]	0.658	0.836	0.909	0.652	0.794
KACE-1–0-G	**0.807**	0.891	0.864	0.673	0.832
MIROC6	0.584	0.817	0.782	**0.822**	0.803
MPI-ESM1-2-HR	**0.798**	0.952	0.879	**0.779**	**0.89**
MPI-ESM1-2-LR	0.575	0.936	0.819	0.752	0.811
MRI-ESM2-0	0.564	0.782	0.867	0.634	0.756
NESM3[a]	0.543	0.922	0.74	0.459	0.777
NorESM2-LM	0.603	0.912	0.882	**0.808**	**0.918**
NorESM2-MM	0.627	0.95	0.869	0.701	0.856
TaiESM1	0.541	0.872	0.821	0.684	0.797
Ensemble	0.611	0.95	0.902	0.84	0.867

Values show the regional average of TSS for the precipitation and temperature annual cycles compared against the ensemble of observations from 1986 to 2014. Bold values show the five best-performed models for Northern Chile (N. CHL), Central Chile (C. CHL), Northern Patagonia (N. Pat), Southern Patagonia (S. Pat), and the entire domain (Chile)

[a]Models with ECS values above the IPCC AR5 likely range (1.5–4.5 °C). 'Hot models' were identified from Tokarska et al. (2020) and Scafetta (2022)

high CMIP6 intermodel agreement (Ukkola et al. 2020). The intensity of these drought events is much stronger and more robust in CMIP6 compared to CMIP5. This trend also extends to Northern Patagonia, which is projected to be affected by an increase in the duration, hydrological deficit, and frequency of severe droughts (Aguayo et al. 2021; Garreaud 2018).

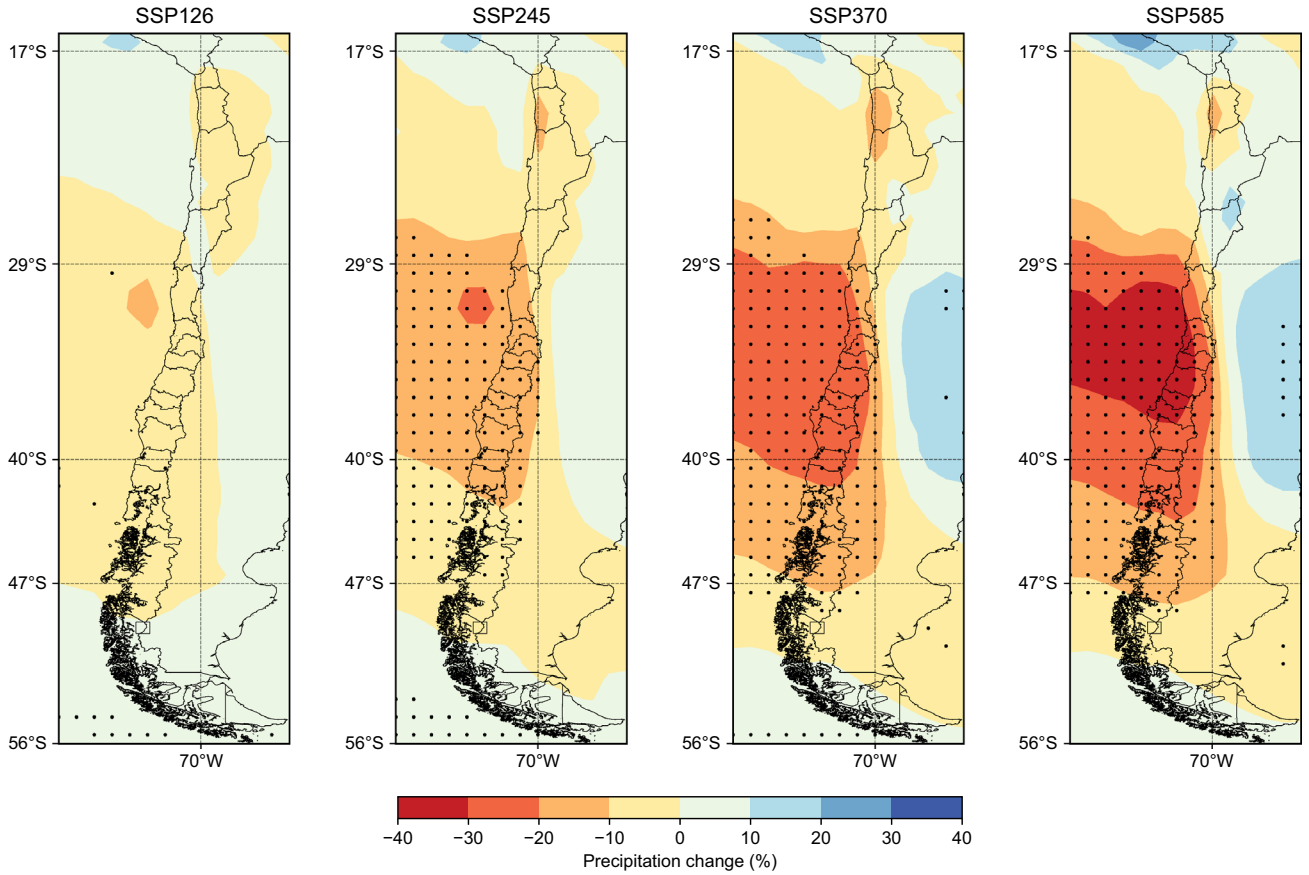

Fig. 10 CMIP6 precipitation change (%) projections for the end of the century under four future emission scenarios. Changes are computed as the ensemble mean for 2080–2099 in relation to the reference period (1986–2014) for 27 models availables for all four scenarios. Black dots represent grid points where at least 90% of GCMs agree on the sign of change. Latitudinal dashed lines show the approximate limits of each subregion (Fig. 1)

Figure 11 shows the temperature projections over Chile from the CMIP6 ensemble. In the case of temperature, we evaluated the strength of changes in sign and magnitude by identifying those grid cells where the projected ensemble mean change is at least twice the standard deviation of the reference period (Almazroui et al. 2021; Scheff and Frierson 2012). In contrast to precipitation, temperature changes incrementally in all models, all subregions and all emission scenarios. CMIP6 projects a mean annual temperature increase between 0 and 2 °C in SSP126, 1–3 °C in SSP245, 1–5 °C in SSP370, and 2–6 °C in SSP585 by the end of the century. Amongst all subregions, Northern Chile displays the greatest increments in temperature ranging from 1–2 °C in the lowest emission scenario to 4–6° in the highest emission scenario, with the maximum change occurring in high mountains. Consistent changes in temperature are present in only a few grid points in SSP370 and over the Andes range in SSP585. The second warmer projection occurs in Central Chile from about 1–1.5 °C in SSP126 to 4–5 °C in SSP585. The strongest increments in mean annual temperature are also presented across the Andes range with a 4–5 °C greater temperature than the reference period. The magnitude of these changes is strong only in the southern portion of the subregion and alongside the coast in the intermediate emission scenario SSP370 and more explicit in the high emission scenario SSP585. This pattern is also present in Northern Patagonia, where pronounced changes in temperature become visible in its meridional extreme in emission scenario SSP370 and widespread in the high emission scenario SSP585. In this scenario, CMIP6 projects a marked increase up to 2–3 °C across all the subregions, with the most significant changes alongside the Andes range. Temperature changes in Southern Patagonia become strong in scenario SSP370 with increments of 2–3 °C and 3–4 °C change over the Andes in the high emission scenario SSP585 (Fig. 11). The projected increase in Andean temperature across subregions might be related to the known elevation-dependent warming (EDW), where high-mountain environments experience more rapid temperature changes than environments at lower elevations (Pepin et al. 2015). Recent evidence of EDW in the Andes of Northern and Central Chile has been reported using observation and modeling approaches

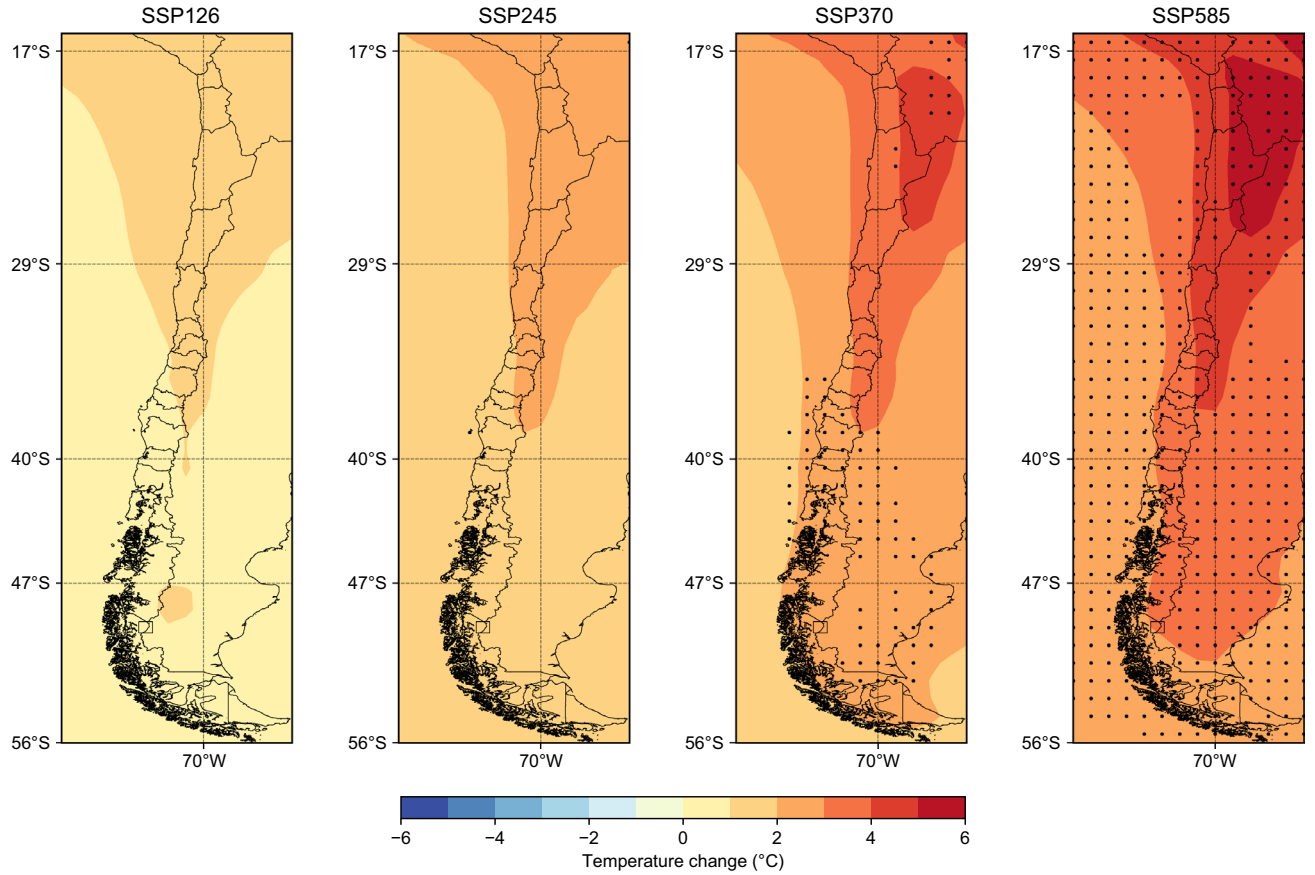

Fig. 11 CMIP6 mean annual temperature change projections (°C) for the end of the century under four future emission scenarios. Changes are computed as the ensemble mean of 2080–2099 in relation to the reference period (1986–2014) for 27 models available for all four scenarios. Black dots represent grid points where temperature changes are greater than twice the standard deviation of the reference period

(Aguilar-Lome et al. 2019; Bambach et al. 2022). Though effective EDW is challenging to validate because sparse high-elevation weather stations and high cloud cover hinder satellite analysis (Pabón-Caicedo et al. 2020), its consequences may significantly impact cryospheric systems, hydrological regimes, ecosystems, settlements, and productive systems.

We finally investigated the relationship between projected precipitation and temperature change for the end of the century in the high-emission scenario SSP585. This is plotted on a two-dimensional space in Fig. 12 and reveals the general pattern of projected changes and the behavior of individual GCMs across different subregions. The trend for sub-regionally averaged change in precipitation and temperature is evident in Central Chile, where GCMs are clustered towards the axis of negative precipitation and positive temperature change ranging from 2.2 to − 37.6% and 2.2 to 5.3 °C, respectively. A clear pattern of change is also visible in Northern Patagonia, where all models project a negative shift in precipitation from − 6.6 to − 31.5% and a positive temperature change from 1.69 to 4.42 °C. For the remaining subregions, the pattern of precipitation change is not conclusive. However, all project positive changes in temperature from 2.85 to 6.15 °C in Northern Chile and from 1.43 to 4.19 °C in Southern Patagonia (Fig. 12).

Interestingly, the GCM that shows the greatest increment in temperature for Central Chile is CanESM5 (5.3 °C), which ranked as the model with the highest TSS value (Table 4). Recently, Rivera and Arnould (2020) reported the same model as the best performing in describing the current precipitation pattern for Central Chile. However, given that CanESM5 is identified as a 'hot model' (Scafetta 2022) its projections must be taken carefully unless model weighting or rescaling the ensemble is applied to avoid highly biased projections (Tokarska et al. 2020). Also, choosing the ensemble with the more reliable models has been proposed (Scafetta 2021). Similarly, the 'hot model' ACCESS-CM2 was the best performing model for Northern Chile, and therefore the same care must be applied in using its raw projections.

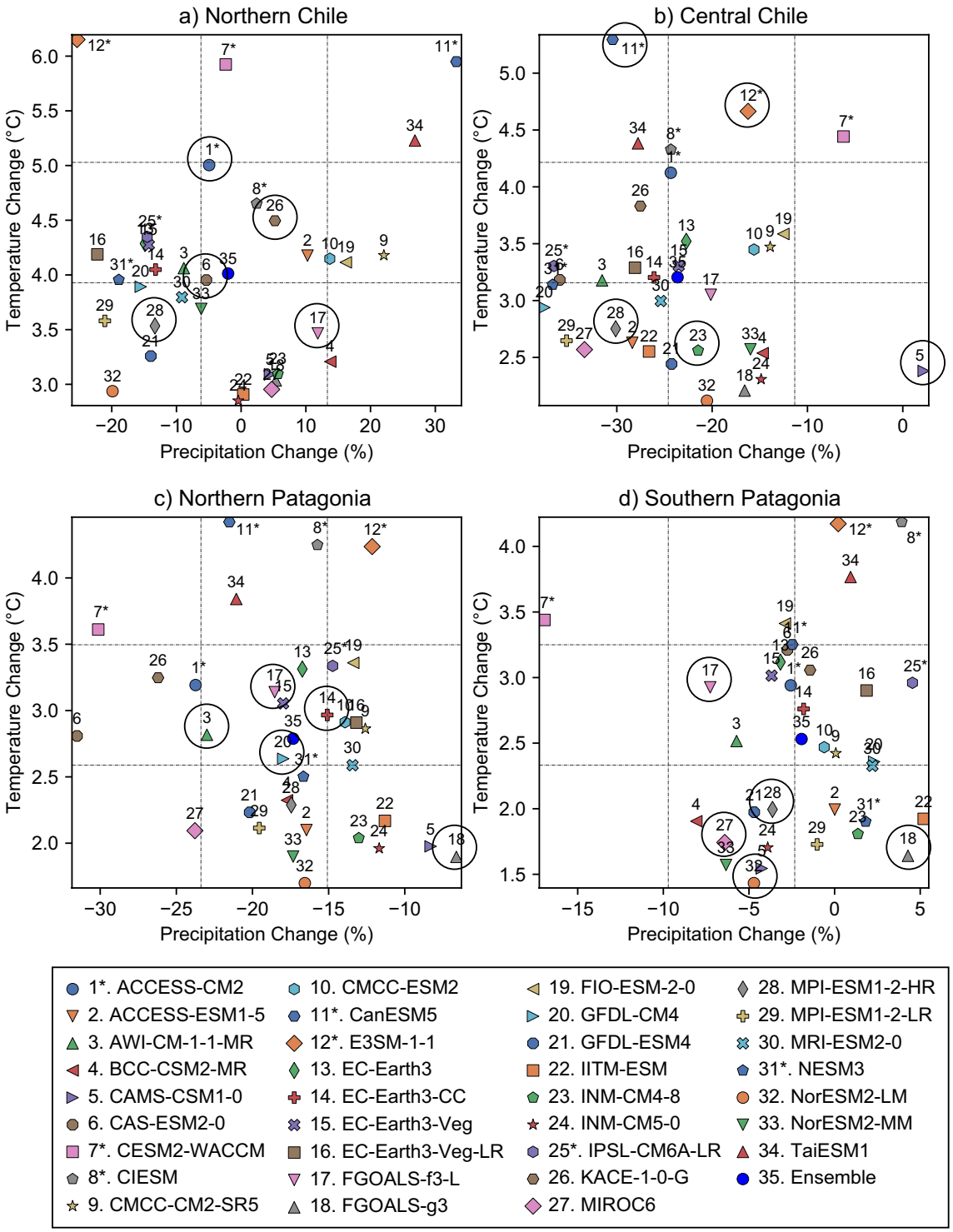

Fig. 12 Precipitation change (%) versus temperature change (°C) over Chile for the end of the century (2080–2099) in relation to the reference period (1986–2014). Change values shown correspond to 34 GCMs available for emission scenario SSP585 spatially averaged over each subregion. Circles represent the top 5 performed models based on the TSS value. 'Hot models' are identified with an asterisk symbol (*)

4 Summary and conclusions

We have evaluated the capability of 36 GCMs from the CMIP6 dataset to reproduce precipitation and temperature against multiple observation datasets for four subregions of Chile and analyzed their projections to the end of the century (2080–2099) in relation to the historical period (1986–2014) for four emission scenarios. A group of metrics was applied to test GCMs in reproducing the temporal and spatial pattern of precipitation and temperature. A ranking was used to identify the models best aligned with observations. Though models can replicate the mean climate, they display varying variability in the spatiotemporal description of precipitation and temperature across subregions. The bias identified in the extremely dry and wet subregions, and the distinct climatic features that characterize Chile's climatic regimes, stress the need to update the reference subregions of the Intergovernmental Panel of Climate Change as proposed in our study. CMIP6 GCMs present warm and wet bias in Northern Chile and Southern Patagonia. Whether this bias is related to the scarcity of ground station data affecting the quality of gridded observations or models' structure and climate variability remains uncertain. We do know these regions have a sparse number of observations and we demonstrate that gridded observations present substantial differences for precipitation and so there is some level of uncertainty in the validation process. Compared to these subregions, Central Chile presents a dense observational network and shows the lowest MBE and NRMSE values. Interestingly, the best models identified based on TSS values for Northern (ACCESS-CM2) and Central Chile (CanESM5) were models with high ECS, and therefore the corresponding projections must be taken cautiously. Though using a large model ensemble (36) may have limited this warm bias, future work should use an ensemble of selected GCMs with realistic values of ECS or a model weighting, among other techniques.

According to CMIP6 models, Central Chile reports one of the greatest future changes in precipitation and temperature and, therefore, represents a climate-change hotspot. The ensemble mean projections for SSP585 scenarios indicate a significantly drier (up to 30–40%) and warmer (up to 4–5 °C) climate that call for an urgent need for the implementation of strong adaptative and mitigation measures during the coming years. The decrease in precipitation becomes robust (in terms of the model agreement on the sign of the changes) from the relatively optimistic scenario SSP245 and is substantial under the highest emission scenario SSP585. Based on our findings, the application of bias correction methods can help decrease the uncertainty of precipitation projections for the Andean areas, particularly in the extremely dry and wet subregions (Beck et al. 2020; Peng et al. 2022). Yet, results might imply an enhancement of precipitation and temperature changes observed during the last decades (Garreaud et al. 2020) and impose additional pressure on an area that supports most of the country's population and industrial production. High-temperature increase in the Andes mountains in all subregions might suggest a significant elevation-dependent warming that can significantly impact Andean snow and ice cover and thus water availability for human consumption, hydropower generation, and the economy (Cordero et al. 2019; Vicuña et al. 2021). The increase in temperature in the studied subregions is expected to accelerate the hydrological cycle and, in combination with the projected precipitation change, can increase the frequency and severity of hydrological and climatological droughts, heat waves, and glacier mass loss acceleration (Ayala et al. 2020; Dussaillant et al. 2019; Pellicciotti et al. 2014). The projected warming can also have severe consequences over the frequency and extension of wildfires (González et al. 2018; Urrutia-Jalabert et al. 2018), affect tree growth decline in remaining natural forests (Matskovsky et al. 2021), change plant community composition in Andean ecosystems by modifying the tree-line frontier in Southern Patagonia (Aguirre et al. 2021) and increase the advent of invasive species in a variety of ecosystems (Schroeder et al. 2023).

As socio-ecological systems' adaptation capacity to a changing climate remains one of the main challenges of the coming decades, we hope that the results presented in this study will help to understand forthcoming climate risks better, support decision-making processes, and further research.

Supplementary Information The online version contains supplementary material available at https://doi.org/10.1007/s00382-023-07034-9.

Author contributions All authors contributed to the study conception and design. Material preparation, data collection and analysis were performed by ÁS and MT. The first draft of the manuscript was written by ÁS and KG and all authors commented on previous versions of the manuscript.

Funding This work was supported by FONDECYT postdoctoral Grant 3190563 and Grant ANID/BASAL FB210006. We also acknowledge the support from FONDECYT 1201742 Grant, Concurso de Fortalecimiento al Desarrollo Científico de Centros Regionales 2020-R20F0008-CEAZA and ANID ACT210046 grant. We thank the climate modeling groups involved in CMIP6 for producing and making available their simulations.

Data availability Data from the Coupled Model Intercomparison Project, Phase 6 (CMIP6) is available at https://esgf-node.llnl.gov/projects/cmip6/. Gridded precipitation data from observations can be accessed at https://www.chc.ucsb.edu/data/chirps (CHIRPS), https://psl.noaa.gov/data/gridded/data.cmap.html (CMAP), https://www.cr2.cl/datos-productos-grillados/ (CR2), https://crudata.uea.ac.uk/cru/data/hrg/cru_ts_4.05/ (CRU), https://disc.gsfc.nasa.gov/datasets/GPCPMON_3.2/summary (GPCP), https://climatedataguide.ucar.edu/clima

te-data/persiann-cdr-precipitation-estimation-remotely-sensed-information-using-artificial (PERSIANN), http://research.jisao.washington.edu/data_sets/ud/ (University of Delaware). Gridded temperature data from observations can be accessed at https://www.cr2.cl/datos-productos-grillados/ (CR2), https://crudata.uea.ac.uk/cru/data/hrg/cru_ts_4.05/ (CRU) and http://research.jisao.washington.edu/data_sets/ud/ (University of Delaware).

Declarations

Conflict of interest The authors have no relevant financial or non-financial interests to disclose.

References

Aguayo R, León-Muñoz J, Garreaud R, Montecinos A (2021) Hydrological droughts in the southern Andes (40–45°S) from an ensemble experiment using CMIP5 and CMIP6 models. Sci Rep. https://doi.org/10.1038/s41598-021-84807-4

Aguilar-Lome J, Espinoza-Villar R, Espinoza J-C, Rojas-Acuña J, Willems BL, Leyva-Molina W-M (2019) Elevation-dependent warming of land surface temperatures in the Andes assessed using MODIS LST time series (2000–2017). Int J Appl Earth Obser Geoinform 77:119–128. https://doi.org/10.1016/j.jag.2018.12.013

Aguirre F, Squeo FA, López D, Grego RD, Buma B, Carvajal D, Jaña R, Casassa G, Rozzi R (2021) Gradientes Climáticos y su alta influencia en los ecosistemas terrestres de la Reserva de la Biosfera Cabo de Hornos, Chile. Anales del Instituto de la Patagonia. https://doi.org/10.22352/aip202149012

Akinsanola AA, Kooperman GJ, Reed KA, Pendergrass AG, Hannah WM (2020) Projected changes in seasonal precipitation extremes over the United States in CMIP6 simulations. Environ Res Lett. https://doi.org/10.1088/1748-9326/abb397

Allen RJ, Kovilakam M (2017) The role of natural climate variability in recent tropical expansion. J Clim 30:6329–6350. https://doi.org/10.1175/JCLI-D-16-0735.1

Almazroui M, Ashfaq M, Islam MN, Rashid IU, Kamil S, Abid MA, O'Brien E, Ismail M, Reboita MS, Sörensson AA, Arias PA, Alves LM, Tippett MK, Saeed S, Haarsma R, Doblas-Reyes FJ, Saeed F, Kucharski F, Nadeem I, Silva-Vidal Y, Rivera JA, Ehsan MA, Martínez-Castro D, Muñoz ÁG, Ali MA, Coppola E, Sylla MB (2021) Assessment of CMIP6 performance and projected temperature and precipitation changes over south America. Earth Syst Environ 5:155–183. https://doi.org/10.1007/s41748-021-00233-6

Alvarez-Garreton C, Pablo Boisier J, Garreaud R, Seibert J, Vis M (2021) Progressive water deficits during multiyear droughts in basins with long hydrological memory in Chile. Hydrol Earth Syst Sci 25:429–446. https://doi.org/10.5194/hess-25-429-2021

Araya-Osses D, Casanueva A, Román-Figueroa C, Uribe JM, Paneque M (2020) Climate change projections of temperature and precipitation in Chile based on statistical downscaling. Clim Dyn 54:4309–4330. https://doi.org/10.1007/s00382-020-05231-4

Ayala Á, Farías-Barahona D, Huss M, Pellicciotti F, McPhee J, Farinotti D (2020) Glacier runoff variations since 1955 in the Maipo River basin, in the semiarid Andes of central Chile. Cryosphere 14:2005–2027. https://doi.org/10.5194/tc-14-2005-2020

Bambach NE, Rhoades AM, Hatchett BJ, Jones AD, Ullrich PA, Zarzycki CM (2022) Projecting climate change in South America using variable-resolution Community Earth System Model: An application to Chile. Int J Climatol 42:2514–2542. https://doi.org/10.1002/joc.7379

Beck HE, Zimmermann NE, McVicar TR, Vergopolan N, Berg A, Wood EF (2018) Present and future Köppen–Geiger climate classification maps at 1-km resolution. Sci Data. https://doi.org/10.1038/sdata.2018.214

Beck HE, Wood EF, McVicar TR, Zambrano-Bigiarini M, Alvarez-Garreton C, Baez-Villanueva OM, Sheffield J, Karger DN (2020) Bias correction of global high-resolution precipitation climatologies using streamflow observations from 9372 catchments. J Clim 33:1299–1315. https://doi.org/10.1175/JCLI-D-19-0332.1

Boisier JP, Rondanelli R, Garreaud RD, Muñoz F (2016) Anthropogenic and natural contributions to the Southeast Pacific precipitation decline and recent megadrought in central Chile. Geophys Res Lett 43:413–421. https://doi.org/10.1002/2015GL067265

Boisier JP, Alvarez-Garreton C, Cordero R, Damian A, Gallardo L, Garreaud R, Lambert F, Ramallo C, Rojas M, Rondanelli R (2018) Anthropogenic drying in central-southern Chile evidenced by long term observations and climate model simulations. Elementa. https://doi.org/10.1525/elementa.328

Bozkurt D, Rojas M, Boisier JP, Valdivieso J (2018) Projected hydroclimate changes over Andean basins in central Chile from downscaled CMIP5 models under the low and high emission scenarios. Clim Change 150:131–147. https://doi.org/10.1007/s10584-018-2246-7

Bozkurt D, Rojas M, Boisier JP, Rondanelli R, Garreaud R, Gallardo L (2019) Dynamical downscaling over the complex terrain of southwest South America: present climate conditions and added value analysis. Clim Dyn 53:6745–6767. https://doi.org/10.1007/s00382-019-04959-y

Cook BI, Mankin JS, Marvel K, Williams AP, Smerdon JE, Anchukaitis KJ (2020) Twenty-first century drought projections in the CMIP6 forcing scenarios. Earths Fut. https://doi.org/10.1029/2019EF001461

Cordero RR, Asencio V, Feron S, Damiani A, Llanillo PJ, Sepulveda E, Jorquera J, Carrasco J, Casassa G (2019) Dry-season snow cover losses in the Andes (18°–40°S) driven by changes in large-scale climate modes. Sci Rep. https://doi.org/10.1038/s41598-019-53486-7

Cos J, Doblas-Reyes F, Jury M, Marcos R, Bretonnière P (2022) The Mediterranean climate change hotspot in the CMIP5 and CMIP6 projections 321–340

Ding Y, Jiang C, Zhou Z, Gao T, Wang S, Zhang X, Cai H, Shi H (2023) Evaluation of precipitation and its time series components in CMIP6 over the Yellow River Basin. Clim Dyn 60(3–4):1203–1223. https://doi.org/10.1007/s00382-022-06379-x

Dussaillant I, Berthier E, Brun F, Masiokas M, Hugonnet R, Favier V, Rabatel A, Pitte P, Ruiz L (2019) Two decades of glacier mass loss along the Andes. Nat Geosci 12:802–808. https://doi.org/10.1038/s41561-019-0432-5

Eyring V, Bony S, Meehl GA, Senior CA, Stevens B, Stouffer RJ, Taylor KE (2016) Overview of the coupled model intercomparison project phase 6 (CMIP6) experimental design and organization. Geosci Model Develop 9:1937–1958. https://doi.org/10.5194/gmd-9-1937-2016

Faye A, Akinsanola AA (2022) Evaluation of extreme precipitation indices over West Africa in CMIP6 models. Clim Dyn 58:925–939. https://doi.org/10.1007/s00382-021-05942-2

Feron S, Asencio V, Llanillo P, Casassa G, Sepulveda E, Jorquera J, Cordero R, Carrasco J, Damiani A (2019) Dry-season snow cover losses in the Andes (18°–40°S) driven by changes in large-scale climate modes. Sci Rep. https://doi.org/10.1038/s41598-019-53486-7

Foley AM (2010) Uncertainty in regional climate modelling: a review. Prog Phys Geogr 34:647–670. https://doi.org/10.1177/0309133310375654

Garreaud R (2009) The Andes climate and weather. Adv Geosci 7:1–9

Garreaud RD (2018) Record-breaking climate anomalies lead to severe drought and environmental disruption in western Patagonia in 2016. Clim Res 74:217–229. https://doi.org/10.3354/cr01505

Garreaud R, Aceituno P (2007) Atmospheric circulation and climatic variability. In: Veblen T, Young K, Orme A (eds) The physical geography of South America

Garreaud R, Vuille M, Clement AC (2003) The climate of the Altiplano: observed current conditions and mechanisms of past changes. In: Palaeogeography, palaeoclimatology, palaeoecology. Elsevier, London, pp 5–22. https://doi.org/10.1016/S0031-0182(03)00269-4

Garreaud R, Vuille M, Compagnucci R, Marengo J (2009) Present-day South American climate. Palaeogeogr Palaeoclimatol Palaeoecol 281:180–195. https://doi.org/10.1016/j.palaeo.2007.10.032

Garreaud R, Molina A, Farias M (2010) Andean uplift, ocean cooling and Atacama hyperaridity: a climate modeling perspective. Earth Planet Sci Lett 292:39–50. https://doi.org/10.1016/j.epsl.2010.01.017

Garreaud R, Lopez P, Minvielle M, Rojas M (2013) Large-scale control on the Patagonian climate. J Clim 26:215–230. https://doi.org/10.1175/JCLI-D-12-00001.1

Garreaud R, Alvarez-Garreton C, Barichivich J, Boisier JP, Christie D, Galleguillos M, LeQuesne C, McPhee J, Zambrano-Bigiarini M (2017) The 2010–2015 megadrought in central Chile: impacts on regional hydroclimate and vegetation. Hydrol Earth Syst Sci 21:6307–6327. https://doi.org/10.5194/hess-21-6307-2017

Garreaud R, Boisier JP, Rondanelli R, Montecinos A, Sepúlveda HH, Veloso-Aguila D (2020) The Central Chile Mega Drought (2010–2018): a climate dynamics perspective. Int J Climatol 40:421–439. https://doi.org/10.1002/joc.6219

Ge F, Zhu S, Luo H, Zhi X, Wang H (2021) Future changes in precipitation extremes over Southeast Asia: insights from CMIP6 multi-model ensemble. Environ Res Lett. https://doi.org/10.1088/1748-9326/abd7ad

Gettelman A, Hannay C, Bacmeister JT, Neale RB, Pendergrass AG, Danabasoglu G, Lamarque JF, Fasullo JT, Bailey DA, Lawrence DM, Mills MJ (2019) High climate sensitivity in the community earth system model version 2 (CESM2). Geophys Res Lett 46:8329–8337. https://doi.org/10.1029/2019GL083978

Ghil M (2020) The physics of climate variability and climate change. Rev Mod Phys 92:35002. https://doi.org/10.1103/RevModPhys.92.035002

Ghil M, Chekroun MD, Simonnet E (2008) Climate dynamics and fluid mechanics: natural variability and related uncertainties. Phys D Nonlinear Phenomena 237:2111–2126. https://doi.org/10.1016/j.physd.2008.03.036

González ME, Gómez-González S, Lara A, Garreaud R, Díaz-Hormazábal I (2018) The 2010–2015 Megadrought and its influence on the fire regime in central and south-central Chile. Ecosphere 9:e02300. https://doi.org/10.1002/ecs2.2300

Grise KM, Davis SM (2020) Hadley cell expansion in CMIP6 models. Atmos Chem Phys 20:5249–5268. https://doi.org/10.5194/acp-20-5249-2020

Grose MR, Narsey S, Delage FP, Dowdy AJ, Bador M, Boschat G, Chung C, Kajtar JB, Rauniyar S, Freund MB, Lyu K, Rashid H, Zhang X, Wales S, Trenham C, Holbrook NJ, Cowan T, Alexander L, Arblaster JM, Power S (2020) Insights from CMIP6 for Australia's future climate. Earth Fut. https://doi.org/10.1029/2019EF001469

Guo H, Bao A, Chen T, Zheng G, Wang Y, Jiang L, de Maeyer P (2021) Assessment of CMIP6 in simulating precipitation over arid Central Asia. Atmos Res. https://doi.org/10.1016/j.atmosres.2021.105451

Gusain A, Ghosh S, Karmakar S (2020) Added value of CMIP6 over CMIP5 models in simulating Indian summer monsoon rainfall. Atmos Res 232:104680. https://doi.org/10.1016/j.atmosres.2019.104680

Hausfather Z, Marvel K, Schmidt GA, Nielsen-Gammon JW, Zelinka M (2022) Climate simulations: recognize the "hot model" problem Setting the agenda in research. Nature 605:26–29

Hu Y, Zhou C, Liu J (2011) Observational evidence for poleward expansion of the Hadley circulation. Adv Atmos Sci 28:33–44. https://doi.org/10.1007/s00376-010-0032-1

Hu D, Jiang D, Tian Z, Lang X (2022) Weakened amplitude and delayed phase of the future temperature seasonal cycle over China during the twenty-first century. Int J Climatol 42(14):7133–7145. https://doi.org/10.1002/joc.7634

Huang J, Yu H, Guan X, Wang G, Guo R (2016) Accelerated dryland expansion under climate change. Nat Clim Chang 6:166–171. https://doi.org/10.1038/nclimate2837

IPCC (2013) The physical science basis. Contribution of working group I to the fifth assessment report of the intergovernmental panel on climate change. Cambridge University Press, Cambridge, United Kingdom and New York, NY, USA

IPCC (2021) Climate change 2021: the physical science basis. Contribution of working group I to the sixth assessment report of the intergovernmental panel on climate change. Cambridge University Press, Cambridge, United Kingdom and New York, NY, USA

IPCC (2022) Climate change 2022. Impacts, adaptation and vulnerability. Contribution of working group II to the sixth assessment report of the intergovernmental panel on climate change. Cambridge University Press, Cambridge, UK and New York, NY, USA

Iturbide M, Gutiérrez JM, Alves LM, Bedia J, Cerezo-Mota R, Cimadevilla E, Cofiño AS, di Luca A, Faria SH, Gorodetskaya IV, Hauser M, Herrera S, Hennessy K, Hewitt HT, Jones RG, Krakovska S, Manzanas R, Martínez-Castro D, Narisma GT, Nurhati IS, Pinto I, Seneviratne SI, van den Hurk B, Vera CS (2020) An update of IPCC climate reference regions for subcontinental analysis of climate model data: definition and aggregated datasets. Earth Syst Sci Data 12:2959–2970. https://doi.org/10.5194/essd-12-2959-2020

Knutti R, Rugenstein MAA (2015) Feedbacks, climate sensitivity and the limits of linear models Subject Areas: Philosophical Transactions A 373, pp 1–20

Knutti R, Allen R, Friedlingstein P, Gregory JM, Hegerl GC, Meehl GA, Meinshausen M, Murphy JM, Pattner GK, Raper SCB, Stocker TF, Stott PA, Teng H, Wigley TML (2008) A review of uncertainties in global temperature projections over the twenty-first century. J Clim 21:2651–2663. https://doi.org/10.1175/2007JCLI2119.1

Kurniadi A, Weller E, Kim Y, Min S (2022) Evaluation of coupled model intercomparison project phase 6 model-simulated extreme precipitation over Indonesia. Int J Climatol. https://doi.org/10.1002/joc.7744

Lambert SJ, Boer GJ (2001) CMIP1 evaluation and intercomparison of coupled climate models. Clim Dyn 17:83–106

Liang Y, Gillett NP, Monahan AH (2020) Climate model projections of 21st century global warming constrained using the observed

warming trend. Geophys Res Lett. https://doi.org/10.1029/2019GL086757
Lun Y, Liu L, Cheng L, Li X, Li H, Xu Z (2021) Assessment of GCMs simulation performance for precipitation and temperature from CMIP5 to CMIP6 over the Tibetan Plateau. Int J Climatol 41:3994–4018. https://doi.org/10.1002/joc.7055
Mardones P, Garreaud RD (2020) Future changes in the free tropospheric freezing level and rain-snow limit: the case of central Chile. Atmosphere 11:1–16. https://doi.org/10.3390/atmos11111259
Massmann AK, Minder JR, Garreaud RD, Kingsmill DE, Valenzuela RA, Montecinos A, Fults SL, Snider JR (2017) The Chilean Coastal orographic precipitation experiment: observing the influence of microphysical rain regimes on coastal orographic precipitation. J Hydrometeorol 18:2723–2743. https://doi.org/10.1175/JHM-D-17-0005.1
Matskovsky V, Venegas-González A, Garreaud R, Roig FA, Gutiérrez AG, Muñoz AA, le Quesne C, Klock K, Canales C (2021) Tree growth decline as a response to projected climate change in the 21st century in Mediterranean mountain forests of Chile. Glob Planet Change. https://doi.org/10.1016/j.gloplacha.2020.103406
Meinshausen M, Nicholls ZRJ, Lewis J, Gidden MJ, Vogel E, Freund M, Beyerle U, Gessner C, Nauels A, Bauer N, Canadell JG, Daniel JS, John A, Krummel PB, Luderer G, Meinshausen N, Montzka SA, Rayner PJ, Reimann S, Smith SJ, Van Den Berg M, Velders GJM, Vollmer MK, Wang RHJ (2020) The shared socio-economic pathway (SSP) greenhouse gas concentrations and their extensions to 2500. Geosci Model Develop 13:3571–3605. https://doi.org/10.5194/gmd-13-3571-2020
Ngoma H, Wen W, Ayugi B, Babaousmail H, Karim R, Ongoma V (2021) Evaluation of precipitation simulations in CMIP6 models over Uganda. Int J Climatol 41:4743–4768. https://doi.org/10.1002/joc.7098
Pabón-Caicedo JD, Arias PA, Carril AF, Espinoza JC, Borrel LF, Goubanova K, Lavado-Casimiro W, Masiokas M, Solman S, Villalba R (2020) Observed and projected hydroclimate changes in the Andes. Front Earth Sci (lausanne). https://doi.org/10.3389/feart.2020.00061
Pellicciotti F, Ragettli S, Carenzo M, McPhee J (2014) Changes of glaciers in the Andes of Chile and priorities for future work. Sci Total Environ. https://doi.org/10.1016/j.scitotenv.2013.10.055
Penalba OC, Rivera JA (2016) Regional aspects of future precipitation and meteorological drought characteristics over Southern South America projected by a CMIP5 multi-model ensemble. Int J Climatol 36:974–986. https://doi.org/10.1002/joc.4398
Peng Y, Duan A, Hu W, Tang B, Li X, Yang X (2022) Observational constraint on the future projection of temperature in winter over the Tibetan Plateau in CMIP6 models. Environ Res Lett 17:1
Pepin N, Bradley RS, Diaz HF, Baraer M, Caceres EB, Forsythe N, Fowler H, Greenwood G, Hashmi MZ, Liu XD, Miller JR, Ning L, Ohmura A, Palazzi E, Rangwala I, Schöner W, Severskiy I, Shahgedanova M, Wang MB, Williamson SN, Yang DQ (2015) Elevation-dependent warming in mountain regions of the world. Nat Clim Chang. https://doi.org/10.1038/nclimate2563
Quintana J, Aceituno P (2012) Changes in the rainfall regime along the extratropical West coast. Atmósfera 25:1–22
Rivera JA, Arnould G (2020) Evaluation of the ability of CMIP6 models to simulate precipitation over Southwestern South America: climatic features and long-term trends (1901–2014). Atmos Res 241:1. https://doi.org/10.1016/j.atmosres.2020.104953
Scafetta N (2021) Testing the CMIP6 GCM simulations versus surface temperature records from 1980–1990 to 2011–2021: high ECS is not supported. Climate 9:1–30. https://doi.org/10.3390/cli9110161
Scafetta N (2022) Advanced testing of low, medium, and high ECS CMIP6 GCM simulations versus ERA5-T2m. Geophys Res Lett 49:1. https://doi.org/10.1029/2022GL097716
Schauwecker S, Aliste V, Ayala Á, Gallardo A, Goubanova K, MacDonell S, Nuñez P, Orrego C, Salazar Á, Segovia A (2023) Current state of snow observations in the semi-arid Andes of Northern Chile: challenges and outlook in view of the current mega-drought. Submitted to Annals of Glaciology—special issue Snow
Scheff J, Frierson D (2012) Twenty-first-century multimodel subtropical precipitation declines are mostly midlatitude shifts. J Clim 25:4330–4347. https://doi.org/10.1175/JCLI-D-11-00393.1
Schroeder L, Robles V, Jara-Arancio P, Lapadat C, Hobbie SE, Arroyo-Kalin M, Cavender-Bares J (2023) Drivers of plant diversity, community composition, functional traits and soil processes along an alpine gradient in the central Chilean Andes. bioRxiv 2023:1. https://doi.org/10.1101/2023.01.13.523936
Shiferaw A, Tadesse T, Rowe C, Oglesby R (2018) Precipitation extremes in dynamically downscaled climate scenarios over the greater horn of Africa. Atmosphere (basel). https://doi.org/10.3390/atmos9030112
Taylor KE (2001) Summarizing multiple aspects of model performance in a single diagram. J Geophys Res Atmos 106:7183–7192. https://doi.org/10.1029/2000JD900719
Tebaldi C, Knutti R (2007) The use of the multi-model ensemble in probabilistic climate projections. Philos Trans R Soc A Math Phys Eng Sci. https://doi.org/10.1098/rsta.2007.2076
Tokarska KB, Stolpe MB, Sippel S, Fischer EM, Smith CJ, Lehner F, Knutti R (2020) Past warming trend constrains future warming in CMIP6 models. Sci Adv 6:9549–9567
Torrez-Rodriguez L, Goubanova K, Muñoz C et al (2023) Evaluation of temperature and precipitation from CORDEX-CORE South America and Eta-RCM regional climate simulations over the complex terrain of Subtropical Chile. Clim Dyn. https://doi.org/10.1007/s00382-023-06730-w
Try S, Tanaka S, Tanaka K, Sayama T (2022) Journal of Hydrology: Regional Studies Comparison of CMIP5 and CMIP6 GCM performance for flood projections in the Mekong River Basin. J Hydrol Region Stud 40:101035. https://doi.org/10.1016/j.ejrh.2022.101035
Ukkola AM, De Kauwe MG, Roderick ML, Abramowitz G, Pitman AJ (2020) Robust future changes in meteorological drought in CMIP6 projections despite uncertainty in precipitation. Geophys Res Lett. https://doi.org/10.1029/2020GL087820
Urrutia-Jalabert R, González ME, González-Reyes Á, Lara A, Garreaud R (2018) Climate variability and forest fires in central and south-central Chile. Ecosphere. https://doi.org/10.1002/ecs2.2171
Viale M, Garreaud R (2014) Summer precipitation events over the western slope of the subtropical andes. Mon Weather Rev 142:1074–1092. https://doi.org/10.1175/MWR-D-13-00259.1
Viale M, Garreaud R (2015) Orographic effects of the subtropical and extratropical Andes on upwind precipitating clouds. J Geophys Res Atmos 120:4962–4974. https://doi.org/10.1002/2014JD023014
Viale M, Bianchi E, Cara L, Ruiz LE, Villalba R, Pitte P, Masiokas M, Rivera J, Zalazar L (2019) Contrasting climates at both sides of the Andes in Argentina and Chile. Front Environ Sci. https://doi.org/10.3389/fenvs.2019.00069
Vicuña S, Vargas X, Boisier JP, Mendoza PA, Gómez T, Vásquez N, Cepeda J (2021) Impacts of climate change on water resources in Chile. In: Fernández B, Gironás J (eds) Water resources of Chile. Springer, Cham, pp 347–363. https://doi.org/10.1007/978-3-030-56901-3_19
Vuille M, Carey M, Huggel C, Buytaert W, Rabatel A, Jacobsen D, Soruco A, Villacis M, Yarleque C, Elison Timm O, Condom T,

Salzmann N, Sicart JE (2018) Rapid decline of snow and ice in the tropical Andes—impacts, uncertainties and challenges ahead. Earth Sci Rev. https://doi.org/10.1016/j.earscirev.2017.09.019

Willmott CJ (1982) Some comments on the evaluation of model performance. Bull Am Meteorol Soc 63:1309–1313

Xia Y, Hu Y, Liu J (2020) Comparison of trends in the Hadley circulation between CMIP6 and CMIP5. Sci Bull (beijing) 65:1667–1674. https://doi.org/10.1016/j.scib.2020.06.011

Xin X, Wu T, Zhang J, Yao J, Fang Y (2020) Comparison of CMIP6 and CMIP5 simulations of precipitation in China and the East Asian summer monsoon. Int J Climatol 40:6423–6440. https://doi.org/10.1002/joc.6590

Zazulie N, Rusticucci M, Raga GB (2018) Regional climate of the Subtropical Central Andes using high-resolution CMIP5 models. Part II: future projections for the twenty-first century. Clim Dyn 51:2913–2925. https://doi.org/10.1007/s00382-017-4056-4